3 Stellar kinematics of $z \sim 2$ galaxies and the inside-out growth of quiescent galaxies

Abstract

Using stellar kinematics measurements, we investigate the growth of massive, quiescent galaxies from $z \sim$2 to today. We present X-Shooter spectra from the UV to NIR and dynamical mass measurements of five quiescent massive ($> 10^{11}\ M_{\odot}$) galaxies at $z \sim 2$. This triples the sample of $z > 1.5$ galaxies with well constrained ($\delta\sigma < 100$km s^{-1}) velocity dispersion measurements. From spectral population synthesis modeling we find that these galaxies have stellar ages that range from 0.5-2 Gyr, with no signs of ongoing star formation. We measure velocity dispersions (290-450 km s^{-1}) from stellar absorption lines and find that they are 1.6-2.1 times higher than those of galaxies in the Sloan Digital Sky Survey at the same mass. Sizes are measured using GALFIT from *Hubble Space Telescope* Wide Field Camera 3 H_{160} and UDS K-band images. The dynamical masses correspond well to the spectral energy distribution based stellar masses, with dynamical masses that are $\sim 15\%$ higher. We find that $M_*/M_{\rm dyn}$ may decrease slightly with time, which could reflect the increase of the dark matter fraction within an increasing effective radius. We combine different stellar kinematic studies from the literature, and examine the structural evolution from $z \sim 2$ to $z \sim 0$: we confirm that at fixed dynamical mass, the effective radius increases by a factor of ~ 2.8, and the velocity dispersion decreases by a factor of ~ 1.7. The mass density within one effective radius decreases by a factor of ~ 20, while within a fixed physical radius (1 kpc) it decreases only mildly (factor of ~ 2). When we allow for an evolving mass limit by selecting a population of galaxies at fixed number density, a stronger size growth with time is found (factor of ~ 4), velocity dispersion decreases by a factor of ~ 1.4, and interestingly, the mass density within 1 kpc is consistent with no evolution. This finding suggests that massive quiescent galaxies at $z \sim 2$ grow inside-out, consistent with the expectations from minor mergers.

Jesse van de Sande, Mariska Kriek, Marijn Franx, Pieter G. van Dokkum,
Rachel Bezanson, Rychard J. Bouwens, Ryan F. Quadri,
Hans-Walter Rix, and Rosalind E. Skelton
The Astrophysical Journal, **771**, 85:110, (2013)

3.1 Introduction

Recent studies have shown that a considerable fraction of massive galaxies at $1.5 < z < 2.5$ have quiescent stellar populations (e.g., Labbé et al. 2005; Kriek et al. 2006; Williams et al. 2009). Among the most massive galaxies ($M_* > 10^{11}\ M_\odot$) approximately 40% are no longer forming stars (e.g., Whitaker et al. 2011; Brammer et al. 2011). Surprisingly, these massive quiescent galaxies have been found to be extremely compact (e.g., Daddi et al. 2005; Trujillo et al. 2006; van Dokkum et al. 2008; Franx et al. 2008; van der Wel et al. 2008; and numerous others), compared to their likely present-day counterparts.

Searches for ultra-dense low-redshift counterparts by Trujillo et al. (2009) and Taylor et al. (2010a) found only a handful of compact sources at $z \sim 0$, which have relatively young stellar populations (Trujillo et al. 2009; Ferré-Mateu et al. 2012). The dearth of massive, old compact objects at low redshift implies that massive galaxies must have undergone severe structural evolution in size.

Errors in the size estimates have been invoked as a possible explanation for the compactness of massive high-redshift galaxies. Initial concerns that the size may have been underestimated, due to an envelope of low surface brightness light, have been addressed with deep *Hubble Space Telescope* Wide Field Camera 3 (*HST*-WFC3) imaging (Szomoru et al. 2010; 2012), and by stacking results (e.g., van der Wel et al. 2008; Cassata et al. 2010; van Dokkum et al. 2008, 2010). The light could also be more concentrated due to the presence of active galactic nuclei (AGNs) in these galaxies. However, spectra of subsamples of these galaxies have shown that the light is dominated by evolved stellar populations, not AGNs (Kriek et al. 2006, 2009; van de Sande et al. 2011; Onodera et al. 2012).

The question of whether stellar masses are accurate out to $z \sim 2$ remains, however, a serious concern: an overestimate in stellar mass would bring the galaxies closer to the $z \sim 0$ mass-size relation. To date, basically all (stellar) masses have been derived by fitting the spectral energy distributions (SEDs). This method suffers from many systematic uncertainties in stellar population synthesis (SPS) models (e.g., Conroy et al. 2009; Muzzin et al. 2009) and is essentially untested at $z > 1.5$.

Direct stellar kinematic mass measurements, which do not suffer from these uncertainties, can be derived by measuring the galaxy's velocity dispersion and the shape and extent of its luminosity profile, i.e., the Sérsic n parameter and effective radius. In particular, for low-redshift galaxies in the Sloan Digital Sky Survey (SDSS), Taylor et al. (2010b) showed that stellar mass is a very good predictor of dynamical mass, but only when non-homology of luminosity profile is properly accounted for using a Sérsic-dependent virial factor (e.g., Cappellari et al. 2006). Although dynamical measurements of massive galaxies are common at low redshift, spectroscopic studies become much more difficult at higher redshift as the bulk of the light, and stellar absorption features used to measure kinematics, shift redward into the near-infrared (NIR; e.g., Kriek et al. 2009; van Dokkum et al. 2009).

New technology such as the new red arm of the LRIS spectrograph at Keck (working beyond 1) makes it possible to measure velocity dispersions up to $z \sim 1.5$ (Newman et al. 2010, Bezanson et al. 2013). Deep NIR spectroscopy is, however, required to push stellar kinematic studies to even higher redshift. From a ∼29 hr spectrum of an ultra-compact galaxy at $z = 2.2$ obtained with Gemini Near-IR Spectrograph (Kriek et al., 2009), van Dokkum et al. (2009) found a high, though uncertain, velocity dispersion of $\sigma = 510^{+165}_{-95}$ km s^{-1}.

Onodera et al. (2012) used the MOIRCS on the Subaru telescope to observe the rest-frame optical spectrum of a less-compact, passive, ultra-massive galaxy at $z = 1.82$, but the low spectral resolution and signal-to-noise ratio (S/N) severely limited the accuracy of their velocity dispersion: $\sigma = 270 \pm 105$ km s^{-1}. X-Shooter (D'Odorico et al. 2006; Vernet et al. 2011), the new Ultraviolet (UV) to NIR spectrograph at the Very Large Telescope (VLT), can provide the required S/N and resolution. The capabilities of X-Shooter for this kind of measurements were demonstrated in van de Sande et al. (2011), who found 294 ± 51 km s^{-1} for a massive quiescent galaxy at $z = 1.8$. Toft et al. (2012) also use X-Shooter and present a dynamical measurement of a galaxy at redshift $z = 2.04$ with similar results. Taken all together, these results indicate that the dynamical and stellar masses are consistent with $z \sim 0$. With the small number of measurements beyond $z > 1.5$, however, the sample is still too small to draw any firm conclusions on whether the stellar masses are truly reliable.

Here we present a sample of five massive quiescent galaxies with high S/N, medium-resolution, UV-NIR spectra at $1.4 < z < 2.1$ observed with X-Shooter on the VLT. The main goal of this chapter will be to test if the stellar mass measurements at high redshift are reliable.

The chapter is organized as follows. In Section 3.2 we, present our sample of high-redshift galaxies, the photometric and spectroscopic data, and describe our data reduction. In Section 3.3 we determine structural properties and stellar populations, and derive stellar and dynamical masses. We complement our results with stellar kinematic results from other studies at low and high redshift in Section 3.4. In Section 3.5, we compare our dynamical to the stellar masses. In Section 3.6 we study the structural evolution of high-redshift quiescent massive galaxies. In Section 3.7, we compare our results with previous measurements and hydrodynamical simulations. Finally, in Section 3.8, we summarize our results and conclusions. Throughout the chapter we assume a ΛCDM cosmology with $\Omega_{\rm m}$=0.3, $\Omega_\Lambda = 0.7$, and $H_0 = 70$ km s^{-1} Mpc^{-1}. All broadband data are given in the AB-based photometric system.

3.2 Data

3.2.1 Target selection

The galaxies in this chapter are drawn from the NMBS-I (Whitaker et al., 2010) and the UKIDSS-UDS (Williams et al., 2009). They were selected to be bright in the H-band, and to have $z > 1.4$, in order to obtain sufficient S/N. The SED from the broadband and medium-band photometry was required to indicate that they have quiescent stellar populations, and the rest-frame optical imaging could not show signs of large disturbance due to e.g., mergers. We note that NMBS-COS7447 was presented in van de Sande et al. (2011), and UDS-19627 was presented in Toft et al. (2012). All data for both galaxies have been re-analyzed according to the following procedure for consistency. Our selection had no priors on mass or size, but could be biased in either one of these parameters. Full information on the photometric properties of the targets is listed in Table 3.1.

To investigate possible biases, we compare our targets to a sample of galaxies with mass $> 10^{10.5} M_\odot$ at $1.4 < z < 2.1$ from the NMBS-I and the UDS. Rest-frame $U-V$ and $V-J$ colors are commonly used to distinguish between star-forming and quiescent galaxies at this

Table 3.1: Photometric properties

Catalog	ID	$J_{\rm aper}$	$H_{\rm aper}$	$K_{\rm aper}$	$K_{\rm tot}$	$(U-V)_{\rm rf}$	$(V-J)_{\rm rf}$	24 μm [μJy]	SFR$_{24\mu m}$ $M_\odot$ yr^{-1}
NMBS-COS	7447	21.09	20.72	20.63	19.64	1.20	0.31	18	13
NMBS-COS	18265	22.67	20.85	20.61	19.62	1.72	0.85	18	15
NMBS-COS	7865	22.75	21.51	21.07	20.02	1.89	0.90	18	19
UDS	19627	21.40	20.91	20.65	20.19	1.37	0.71	30	29
UDS	29410	20.59	20.18	19.81	19.36	1.62	0.96	232 ± 15	241 ± 16

Aperture and total magnitudes for our targets. Aperture magnitudes have been measured in fixed 1.5 arcsec diameter aperture for targets in NMBS-I, while the targets in UDS have 1.75 arcsec diameter apertures. Rest-frame colors have been derived from the spectra in Johnson U, V, and $2MASSJ$ filters. For the 24 μm fluxes we provide 3-σ upper-limits of 18 μJy for the galaxies in NMBS-COSMOS (Whitaker et al., 2012), and 30 μJy for UDS-19627 (Toft et al., 2012), as these galaxies are not detected with MIPS. UDS-29410 has a strong MIPS detection, which is likely due to an obscured AGN.

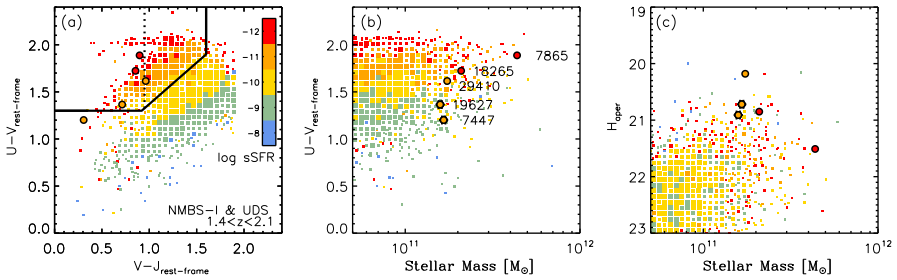

Figure 3.1: Comparison of our spectroscopic sample to the full population at similar redshift. Symbol size of the squares represent the density of galaxies from the NMBS-I and UDS at $1.4 < z < 2.1$ with mass $> 10^{10.5} M_\odot$. (a) Rest-frame U-V and V-J colors. Color coding is based upon the sSFR derived from SED fitting, red colors indicate low sSFR (quiescent), and blue colors indicate high sSFR(star-forming). Galaxies in the top left region, as marked by the black line, all have low sSFR rates. This region is therefore often used to select quiescent galaxies at high redshift (Williams et al., 2009). All but one of our galaxies fall within this region, but their sSFR indicate that they are all have quiescent stellar populations. The vertical dotted line discriminates between young post-starburst like (left) vs. old quiescent (right) as indicated by Whitaker et al. (2012). The strong Balmer absorption lines spectroscopically confirm the young ages of this sample. (b) Rest-frame U-V vs. stellar mass. At fixed mass, we find that most of our galaxies have similar colors to the entire population, except for NMBS-COS7447 and UDS-19627 on the blue side. (c) H-band aperture magnitude vs. stellar mass. It is clear that our sample was selected on magnitude, and at fixed mass they are among the brightest galaxies, consistent with their post-starburst nature.

redshift (e.g., Williams et al. 2009). Figure 3.1(a) shows the UVJ-diagram for all galaxies at redshifts between $1.4 < z < 2.1$ with mass $> 10^{10.5} M_\odot$, together with the sample presented here. The sizes of the squares indicate the density of galaxies. For our targets, the rest-frame colors have been measured from the spectra, while for the full sample rest-frame colors are based on the broadband and medium-band data. As demonstrated by Williams et al. (2009), non-star-forming galaxies can be identified using a color selection indicated by the black lines. Within this selection region, our targets fall in the area occupied by young, quiescent galaxies (Whitaker et al., 2012).

Table 3.2: Targets and observations

Catalog	ID	R.A.	Dec.	Exp. Time [min]	Slit Size NIR [arcsec]	S/N J [Å^{-1}]	S/N H [Å^{-1}]	S/N $_{4020<\lambda}$ Å<7000 [Å^{-1}]	Telluric Standard Star $Hipparcos\ ID$
NMBS-COS	7447	10:00: 6.96	2:17:33.77	120	0.″9	4.98	8.48	6.31	050307, 000349
NMBS-COS	18265	10:00:40.83	2:28:52.15	90	0.″9	3.37	6.99	4.18	050684, 000349
NMBS-COS	7865	10:00:17.73	2:17:52.75	434	0.″9	1.64	5.86	4.12	049704, 057126, 046054, 040217, 059987
UDS	19627	2:18:17.06	-5:21:38.83	300	0.″6, 0.″9	3.80	7.94	5.90	012377, 114656, 008352, 000328, 015389
UDS	29410	2:17:51.22	-5:16:21.84	120	0.″9	3.75	7.09	4.35	012377

R.A. and Dec. are given in the J2000 coordinate system. Exposure times are given for the NIR arm, the UVB and VIS arms had slightly shorter exposure times due to the longer read out. Except for UDS19627, all targets were observed with a 0.″9 slit in the NIR. S/N ratios have been determined from comparing the residual of the velocity dispersion fit to the flux, and are given for the $J-$ and $H-$band as well as for the region in which we determine the velocity dispersion. Last column gives the Tellurics Standard Stars from the Hipparcos catalog that were observed before and after each target.

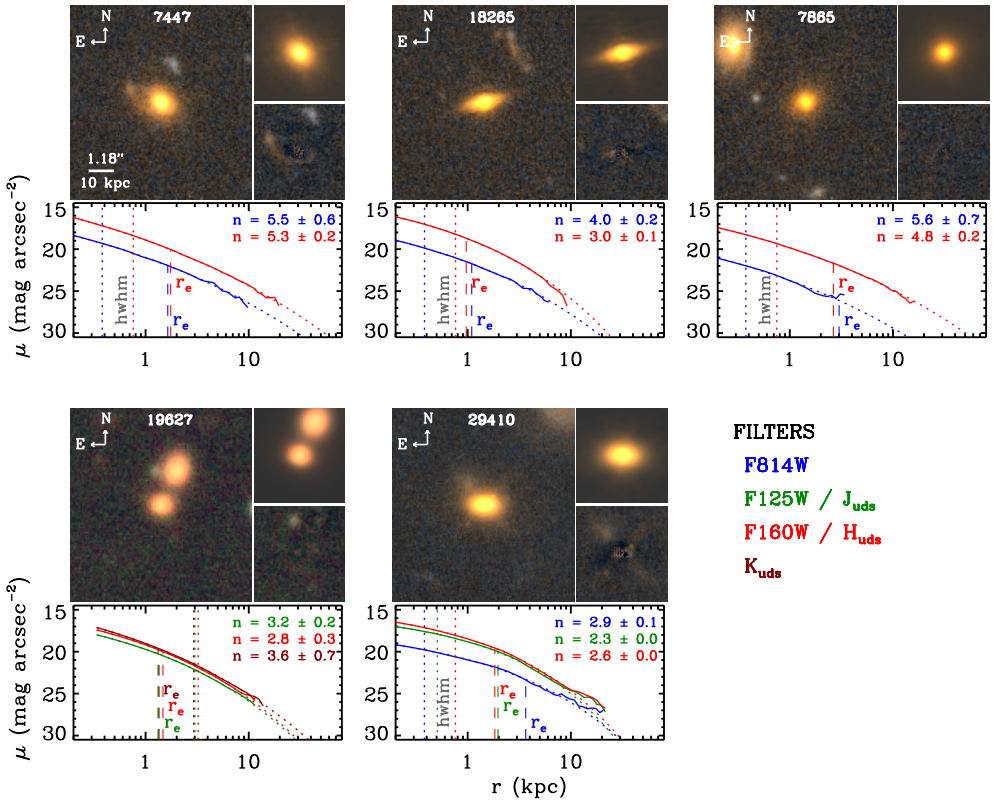

Figure 3.2: Color images of our five spectroscopic targets. Except for UDS-19627, all galaxies have available *HST*-WFC3 Imaging. For each target we show the composite color image on the left side, the best Sérsic model from GALFIT and the residual after we subtract the best-fitting model from the original image on the right side. The lower panel shows the intrinsic surface brightness profile with all available bands. Different colors show the different filters, as indicated on the bottom right. Vertical dashed lines show the effective radii for each profile, while the dotted lines shows the FWHM/2 of the PSF. We find color gradients, such that the redder bands have smaller effective radii, for all galaxies but NMBS-COS7447. For that case, the sizes are similar within the errors, but this could be caused by the extra flux of the red arc-like feature in the southeast.

The median specific star formation rates (sSFR), as indicated by the different colors, are in good agreement with the full high-redshift sample at the same place in the UVJ diagram. For their mass, however, NMBS-COS7447 and UDS-19627 have slightly bluer colors as compared to the full sample (Figure 3.1(b)). At fixed mass, the targets are among the brightest galaxies, except for NMBS-I-7865 (3.1(c)). This may not come as a surprise as they are among the youngest quiescent galaxies, and thus have relatively low M/L.

3.2.2 Imaging

Four different imaging data sets are used to measure the surface brightness profiles of our galaxies, as summarized below. (1) All our targets in the NMBS-I COSMOS field were ob-

served with *HST*-WFC3 H_{160} as part of the program *HST*-GO-12167 (PI: Franx). Each target was observed for one orbit (2611 sec), using a four point dither pattern, with half pixel offsets. Reduction of the data was done in a similar way as to the reduction described in Bouwens et al. (2010), but without sigma-clipping in order to avoid masking the centers of stars. The drizzled images have a pixel scale of $0\farcs06$, with a full width at half-maximum (FWHM) of the point-spread function (PSF) of $\sim 0\farcs16$. (2) Our NMBS-I targets are complemented with *HST*-ACS I_{814} imaging from COSMOS (v2.0, Koekemoer et al. 2007; Massey et al. 2010), which has a $0\farcs03$ pixel scale and PSF-FWHM of $\sim 0\farcs11$. (3) For UDS-29410 we make use of the *HST*-ACS F814W, *HST*-WFC3 J_{125} and H_{160} from UDS-CANDELS (Grogin et al. 2011; Koekemoer et al. 2011). These data have the same properties as the data described in (1) and (2). (4) For UDS-19627 we use ground based data from UKIDSS-UDS, (Lawrence et al. 2007; Warren et al. 2007) Data Release 8 in the J, H, and K-band, as no as *HST* data is available. Imaging in all three bands were drizzled to a pixel scale $0\farcs134$, and the FWHM of the PSF is $0\farcs7$ in the K-band.

3.2.3 Spectroscopic observations

Observations were performed with X-Shooter on the VLT UT2 (D'Odorico et al. 2006; Vernet et al. 2011). X-Shooter is a second generation instrument on the VLT that consists of three arms: UVB, VIS, and NIR. The wavelength coverage ranges from 3000 Å to 24800 Å in one single exposure. The galaxies were observed in both visitor and service mode, and the observations were carried out between 2010 January and 2011 March (Programs: Fynbo 084.A-0303(D), Van de Sande 084.A-1082(A), Franx 085.A-0962(A), Toft 086.B-0955(A)). Full information on the targets and observations is listed in Table 3.2. All observations had clear sky conditions and an average seeing of $0\farcs8$. A $0\farcs9$ slit was used in the NIR, except for the 1st hour of UDS-19627 where a $0\farcs6$ slit was used. For the $0\farcs9$ slit, this resulted in a spectral resolution of 5100 at 1.4μm. Observing blocks were split into exposures of 10-15 minutes each with an $ABA'B'$ on-source dither pattern. For most targets, a telluric standard of type B8V-B9V was observed before and after our primary target, in order to create a telluric absorption spectrum at the same airmass as the observation of our target.

3.2.4 Spectroscopic reduction

Data from the three arms of X-Shooter must be analyzed separately and then combined to cover the full range from the UV to NIR. In the NIR we identified bad pixels in the following way. The data were corrected for dark current, flatfielded, and sky subtracted using the average of the preceding and subsequent frames. The ESO pipeline (ver. 1.3.7; Goldoni et al. 2006) was used to derive a wavelength solution for all orders. The orders were then straightened using integer pixel shifts to retain the pixels affected by cosmic-rays and bad pixels. Additional sky subtraction was done on the rectified orders, by subtracting the median in the spatial direction. Cosmic rays and bad pixels were identified by LA-Cosmic (van Dokkum & Franx, 2001), and a bad pixel mask was created.

Further 3σ clipping was done on the different exposures, corrected for dithers, to identify any remaining outliers. The bad pixel masks of different orders were combined into a single

Table 3.3: Stellar population synthesis properties

Catalog	ID	z_{phot}	z_{spec}	$\log \tau$ (yr)	$\log Age$ (yr)	Z	A_V (mag)	$\log M_*$ ($M_\odot$)	log SFR ($M_\odot \mathrm{yr}^{-1}$)	log sSFR (yr^{-1})
NMBS-COS	7447	1.71± 0.03	1.800	7.80	8.74	0.020	0.00	11.27	-0.08	-11.35
NMBS-COS	18265	1.60± 0.03	1.583	7.00	8.96	0.020	0.45	11.42	-99.00	-99.00
NMBS-COS	7865	2.02± 0.05	2.091	7.20	9.41	0.008	0.05	11.68	-99.00	-99.00
UDS	19627	1.94± 0.06	2.036	7.90	8.74	0.050	0.20	11.24	0.56	-10.68
UDS	29410	1.44± 0.02	1.456	7.90	8.82	0.050	0.35	11.29	-99.00	-11.28

Derived stellar population synthesis properties from FAST. We use stellar templates from Bruzual & Charlot 2003, with an exponentially declining star formation history with timescale τ, together with a Chabrier (2003) IMF, and the Calzetti et al. (2000) reddening law. No errors are provided, as the 68% confidence all fall within one grid point. The real errors are dominated by systematic uncertainties.

file and then transformed back to the raw frame for each exposure. Masks will follow the same rectification and wavelength calibration steps as the science frames.

Next the flatfielded and sky subtracted observations were rectified and wavelength calibrated, only this time we used interpolation when rectifying the different orders. Again, additional sky subtraction was done. Per order, all exposures were combined, with exclusion of bad pixels and those contaminated with cosmic rays present in the mask file.

The telluric spectra were reduced in the same way as the science frames. We constructed a response spectrum from the telluric stars in combination with a stellar model for a B8V/B9V star from a blackbody curve and models from Munari et al. (2005). Residuals from Balmer absorption features in the spectrum of the tellurics were removed by interpolation. All the orders of the science observations were corrected for instrumental response and atmospheric absorption by dividing by the response spectrum.

The different orders were then combined, and in regions of overlap weighted using the S/N of the galaxy spectrum. A noise spectrum was created by measuring the noise in the spatial direction below and above the galaxy. If the regions exceeded an acceptable noise limit, from contamination by OH lines or due to low atmospheric transmission, this spatial region was discarded for further use. The two-dimensional (2D) spectra were visually inspected for emission lines, but none were found. A one-dimensional (1D) spectrum was extracted by adding all lines (along the wavelength direction), with flux greater than 0.1 times the flux in the central row, using optimal weighting.

Absolute flux calibration was performed by scaling the spectrum to the available photometric data. The scaling was derived for each individual filter that fully covered the spectrum. For our targets in NMBS-I we used the following filters: $J, J2, J3, H, H1, H2$, and, Ks, while for the targets in the UDS we only used J and H. We then used an error-weighted average obtained from the broadband magnitudes, and scaled the whole spectrum using this single value. After scaling, no color residuals were found, and no further flux corrections were applied to the spectrum.

A low resolution spectrum was constructed by binning the 2D spectrum in wavelength direction. Using a bi-weight mean, 20 good pixels, i.e., not affected by skylines or strong atmospheric absorption, were combined. The 1D spectrum was extracted from this binned

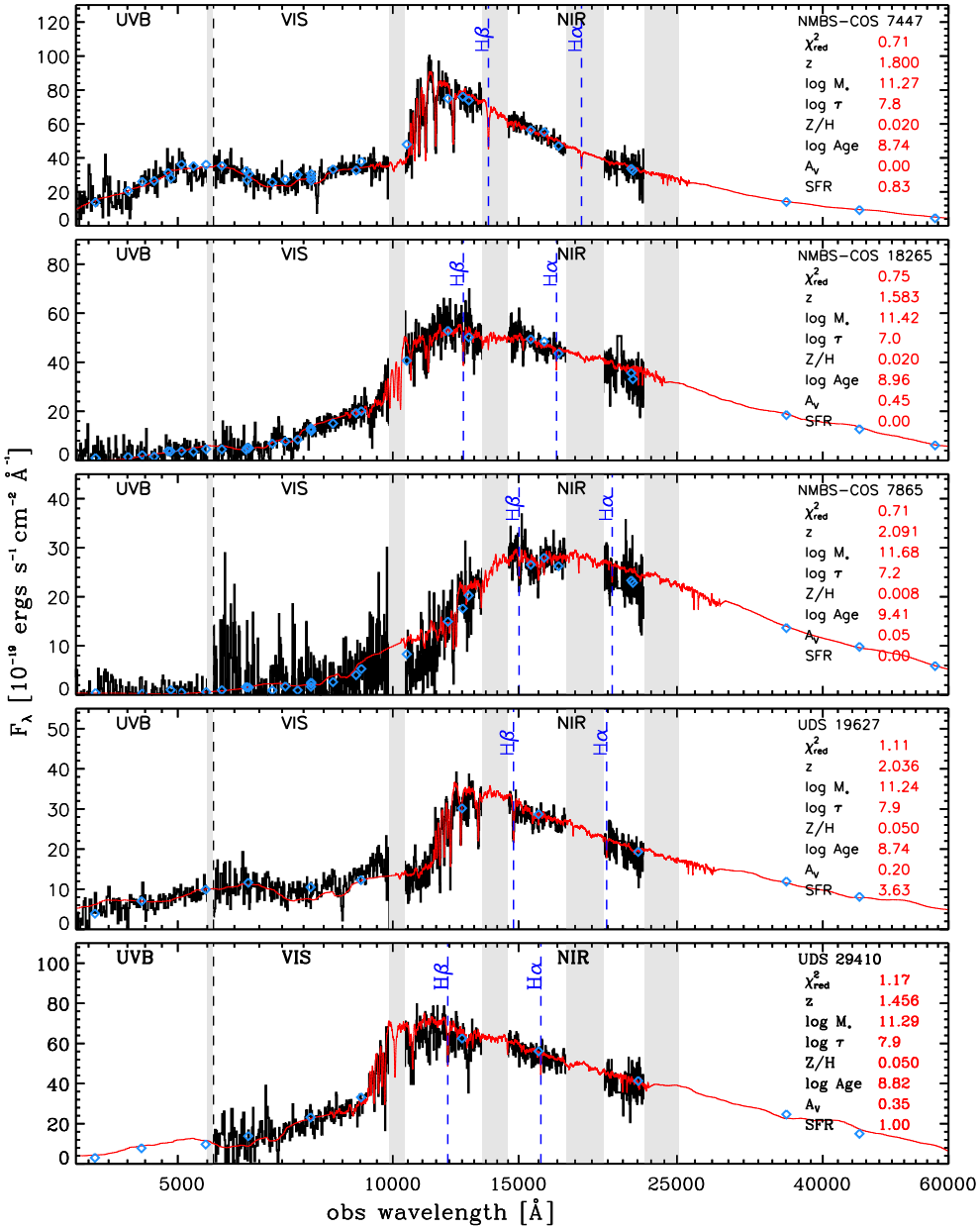

Figure 3.3: UV to NIR X-Shooter spectra in combination with medium- and broad-band data (blue diamonds). The binned spectra ($\sim$ 10 Å) are shown in black, together with the best-fitting BC03 τ-model as shown in red. Gray areas indicate regions with strong atmospheric absorption. The UVB spectrum is missing for UDS-29410, due to an instrument problem during the observations. The good agreement between the BC03 models and the spectroscopic data over this large wavelength range is astonishing. Both NMBS-COS7865 and UDS-19627 show a small deviation from the best-fitting model around 1, which is caused by the absence of good telluric calibrators. From stellar population synthesis modeling, we find a variety of ages that range from 0.5-2 Gyr. We find no emission lines, and other signs of star formation, and with little to no dust (see Section 3.3.1).

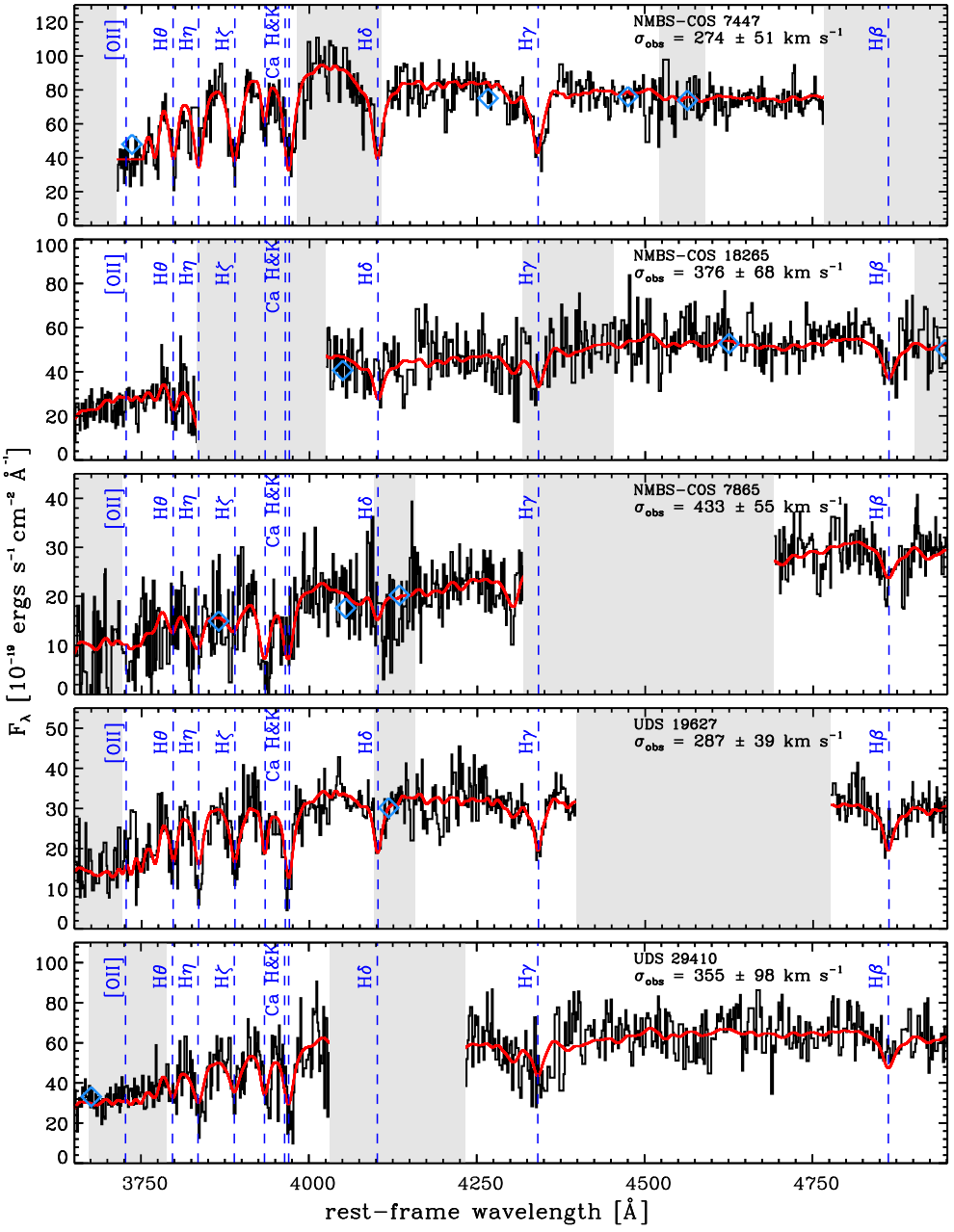

Figure 3.4: Rest-frame optical part of the spectrum focused on the Balmer break. As in Figure 3.3, the X-Shooter spectrum is shown in black, but this time in higher resolution ($\sim$ 4 Å observed, or $\sim$ 100 km s^{-1} rest-frame). The most prominent absorption and emission features are indicated by the blue dashed lines. The clear detection of absorption lines enables us to measure stellar velocity dispersions. We use pPXF to fit the best-fitting BC03 τ model to the spectrum and find velocity dispersions that range from 275-435 km s^{-1}. The convolved best-fit BC03 template is shown in red.

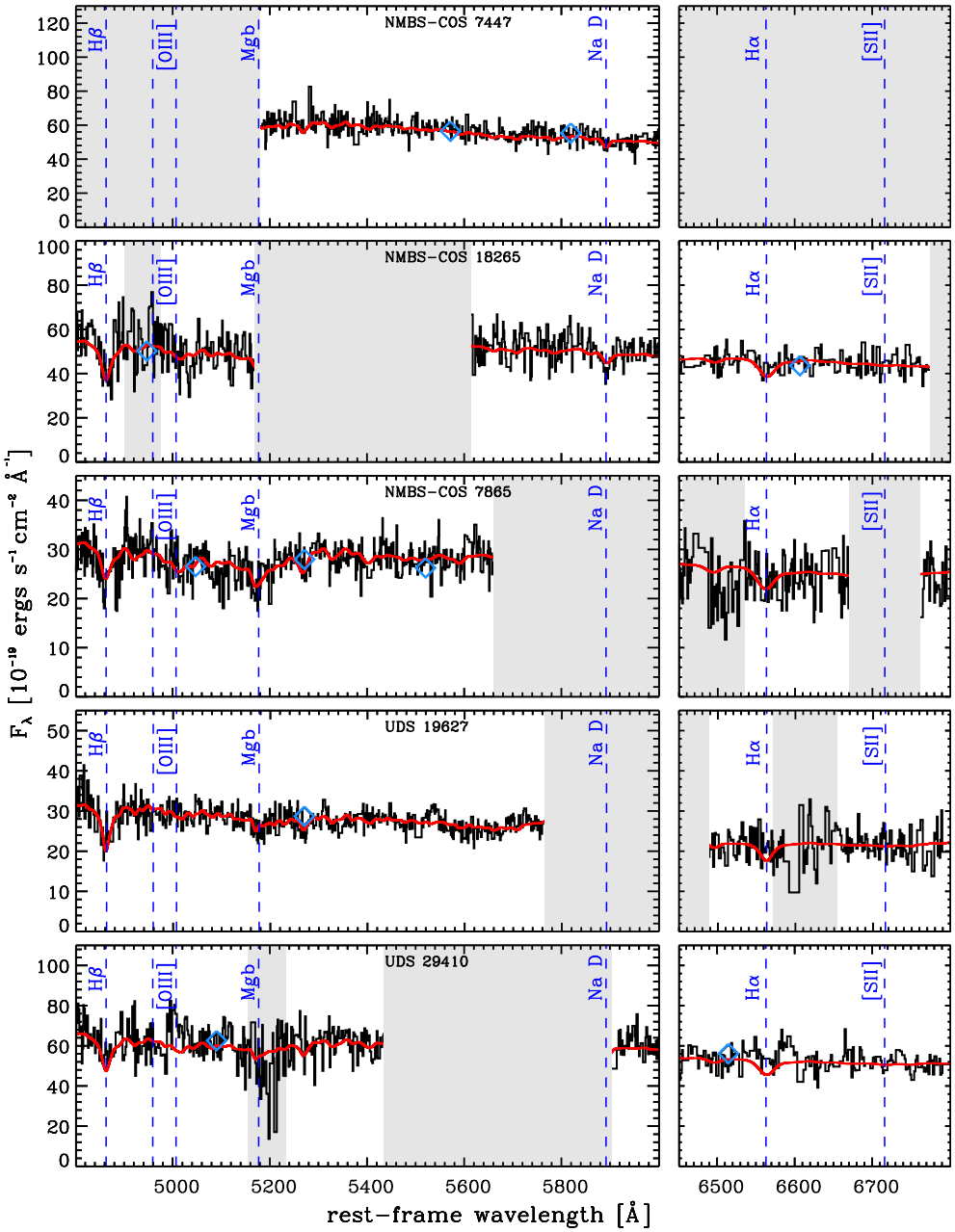

Figure 3.5: Rest-frame optical part of the spectrum focused on Mgb, NaD, and $H\alpha$. As in Figure 3.4, the X-Shooter spectrum is shown in black, with high resolution of $\sim$ 4 Å observed, or $\sim$ 100 km s^{-1} rest-frame. The most prominent absorption and emission features are indicated by the blue dashed lines. The convolved best-fit BC03 template is shown in red.

2D spectrum in a similar fashion as the high resolution spectrum *(see Figure 3.3 - 3.5)*.

For the UVB and VIS arms we used the ESO reduction pipeline (ver 1.3.7, Goldoni et al. 2006) to correct for the bias, flatfield, and dark current, and to derive the wavelength solution. The science frames were also rectified using the pipeline, but thereafter, treated in exactly the same way as the rectified 2D spectra of the NIR arm, as described above.

3.3 Structural properties and stellar populations

3.3.1 Stellar population properties

We estimate the stellar population properties by fitting the low-resolution ($\sim 10\,$Å in the observed frame) spectrum in the visual and NIR in combination with the broadband and medium-band photometry with SPS models. We exclude the UVB part of the spectrum due to the lower S/N and the extensive high S/N broadband photometry in this wavelength region. Stellar templates from Bruzual & Charlot (2003, BC03) are used, with an exponentially declining star formation history (SFH) with timescale τ, together with a Chabrier (2003) initial mass function (IMF), and the Calzetti et al. (2000) reddening law.

Using the FAST code (Kriek et al., 2009), we fit a full grid in age, dust content, star formation timescale, and metallicity. We adopt a grid for τ between 10 Myr and 1 Gyr in steps of 0.1 dex. The age range can vary between 0.1 Gyr and 10 Gyr, but the maximum age is constrained to the age of the universe at that particular redshift. We note, however, that this constraint has no impact on our results as the galaxies are young. Step size in age is set as high as the BC03 templates allow, typically 0.01 dex. Metallicity can vary between $Z = 0.004$ (subsolar), $Z = 0.08$, $Z = 0.02$(solar), and $Z = 0.05$ (supersolar). Furthermore, we allow dust attenuation to range from 0 to 2 mag with step size of 0.05. The redshift used here is from the best-fitting velocity dispersion (see Section 3.3.2). Results are summarized in Table 3.3.

Due to our discrete grid and the high quality data, and also because metallicity and age are limited by the BC03 models, our 68% confidence levels are all within one grid point. Our formal errors are therefore mostly zero, and not shown in Table 3.3. This does not reflect the true uncertainties, which are dominated by the choice of SPS models, IMF, SFH, and extinction law (see, e.g., Conroy et al. 2009; Muzzin et al. 2009).

The low sSFR confirms the quiescent nature of the galaxies in our sample, and they match well with the sSFR of the general population in the same region of the UVJ diagram (Figure 3.1(a)). We find a range of metallicities, with the oldest galaxy having the lowest metallicity. However, due to the strong degeneracy between age and metallicity, we do not believe this result to be significant. Overall, the dust content in our galaxies is low.

We find very similar results for NMBS-C7447 as compared to van de Sande et al. (2011), and the small differences can be explained by the newer reduction. For UDS-19627 we find a slightly lower mass as compared to Toft et al. (2012), which is likely due to the lower dust fraction that we find, i.e., $A_v = 0.2$ vs. $A_v = 0.77$ from Toft et al. (2012).

Table 3.4: Compilation of masses and structural parameters for high-redshift galaxies

Reference[a]	ID	z_{spec}	r_e	n_{sersic}	b/a	σ_e	σ_e/σ_{ap}	$\beta(n)$	$\log M_{dyn}$	$\log M_{*,corr}$	Filter
0	7447	1.800	1.75 ± 0.21	5.27 ± 0.23	0.71 ± 0.02	287^{+55}_{-52}	1.048	5.16	$11.24^{+0.13}_{-0.12}$	11.22	$H_{\rm F160W}$
0	18265	1.583	0.97 ± 0.12	2.97 ± 0.06	0.26 ± 0.02	400^{+78}_{-66}	1.065	6.61	$11.38^{+0.13}_{-0.11}$	11.32	$H_{\rm F160W}$
0	7865	2.091	2.65 ± 0.33	4.82 ± 0.15	0.83 ± 0.02	446^{+54}_{-59}	1.031	5.42	$11.82^{+0.09}_{-0.09}$	11.64	$H_{\rm F160W}$
0	19627	2.036	1.32 ± 0.17	3.61 ± 0.73	0.48 ± 0.06	304^{+43}_{-39}	1.059	6.18	$11.24^{+0.10}_{-0.09}$	11.20	K
0	29410	1.456	1.83 ± 0.23	2.59 ± 0.03	0.54 ± 0.02	371^{+114}_{-90}	1.045	6.88	$11.61^{+0.19}_{-0.15}$	11.24	$H_{\rm F160W}$
.....	.....	.....	.....	.....	.....	.....	.....	.....	.....	.....	.....

This Table will be published in its entirety in the electronic edition of ApJ, and can also be downloaded from `http://www.strw.leidenuniv.nl/~sande/data/`. A portion is shown here for guidance regarding its form and content. Spectroscopic redshifts z_{spec} are obtained from the velocity dispersion fit as described in Section 3.3.2. Structural parameters r_e, n_{sersic}, and b/a are derived using GALFIT on available imaging, as described in Section 3.3.3. σ_e is the velocity dispersion within a circular aperture of size r_e from Section 3.3.2, and σ_e/σ_{ap} is the aperture correction we apply to the observed velocity dispersion as described in Appendix 3.B. From Equation 3.2 we calculated $\beta(n)$, and dynamical masses are derived using Equation 3.1. Stellar masses as given here are corrected to account for the difference between the catalog magnitude and our measured magnitude. The filter in which the structural parameters are measured is given in the last column.
(a) References: 0) this work 1) Bezanson et al. (2013); 2) van Dokkum et al. (2009); 3) Onodera et al. (2012); 4) Cappellari et al. (2009); 5) Newman et al. (2010); 6) van der Wel et al. (2008) and Blakeslee et al. (2006); 7) Toft et al. (2012).

The galaxies in our sample are not detected at 24 μm, leading to a 3-σ upper-limit of 18 μJy for the galaxies in NMBS-COSMOS, and 30 μJy for UDS-19627 (see Whitaker et al. 2012; Toft et al. 2012). UDS-29410 has a strong detection at 24 μm of $232 \pm 15 \mu Jy$. From these upper limits we calculate the dust-enshrouded SFRs that are listed in Table 3.2. We find a high SFR for UDS-29410, but we find no other signs for this high SFR. That is, we find no emission lines and the best fitting SPS model indicates a low SFR. Therefore, we think that the strong 24 μm detection is likely due to an obscured AGN.

3.3.2 Velocity dispersions

The clear detection of absorption lines in our spectra, together with the medium resolution of X-Shooter, enable the measurement of accurate stellar velocity dispersions. We use the unbinned spectra in combination with the Penalized Pixel-Fitting (pPXF) method by Cappellari & Emsellem (2004) and our best-fitting BC03 models as templates. Spectra were resampled onto a logarithmic wavelength scale without using interpolation, but with masking of the bad pixels. The effect of template mismatch was reduced by simultaneously fitting the template with a $\sim$17-order Legendre Polynomial. Our results depend only slightly on the choice of the order of the polynomial (Appendix 3.A). Together with the measured velocity dispersion, the fit also gives us the line-of-sight velocity, and thus $z_{\rm spec}$.

We also look at dependence of the velocity dispersion on the template choice. In particular for the younger galaxies in our sample that show a clear signature of A-type stars, we find a dependence of the measured velocity dispersion as a function of template age. A more stable fit is obtained when restricting the wavelength range to $4020\,\text{Å} < \lambda < 7000\,\text{Å}$, which excludes the Balmer break region (see also Appendix 3.A).

The errors on the velocity dispersion were determined in the following way. We subtracted the best-fit model from the spectrum. Residuals are shuffled in wavelength space and added to the best-fit template. We then determined the velocity dispersion of 500 of these simulated spectra. Our quoted error is the standard deviation of the resulting distribution of the measured velocity dispersions. When we include the Balmer break region in the fit, the formal random error decreases, but the derived dispersion becomes more dependent on the chosen stellar template. In total we have three high-quality measurements, and two with medium quality. We note that if we exclude the two galaxies with medium-quality measurements from our sample, our main conclusions would not change.

The velocity dispersion found here for NMBS-C7447 agrees well with the results from van de Sande et al. (2011). For UDS-19627 we find a slightly lower value as compared to Toft et al. (2012). However, they use a different method for constructing the template for the velocity dispersion fit. When we fit the spectrum of UDS-19627 in the same way as was described in Toft et al. (2012), we find a similar answer as theirs.

All dispersions are corrected for the instrumental resolution (σ=23 km s^{-1}) and the spectral resolution of the templates (σ=85 km s^{-1}). Furthermore, we apply an aperture correction to our measurements as if they were observed within a circular aperture radius of $r_{\rm e}$. In addition to the traditional correction for the radial dependence of velocity dispersion (e.g., Cappellari et al. 2006), we account for the effects of the non-circular aperture, seeing and optimal extraction of the 1-D spectrum. The aperture corrections are small with a median of 4.8% (See Appendix 3.B). The final dispersions and corresponding uncertainties are given in Table 3.4.

3.3.3 Surface brightness profiles

Radial profiles are measured for all galaxies on all available imaging as described in Section 3.2.2. Galaxies are fitted by 2D Sérsic radial surface brightness profiles (Sérsic, 1968), using GALFIT (ver. 3.0.2; Peng et al. 2010). Relatively large cutouts of $25'' \times 25''$ were provided to GALFIT to ensure an accurate measurement of the background, which was a free parameter in the fit. All neighboring sources were masked using a segmentation map obtained with SExtractor (Bertin & Arnouts, 1996). In the case of UDS-19627, the close neighbor was fitted simultaneously. Bright unsaturated field stars were used for the PSF convolution. All parameters, including the sky, were left free for GALFIT to determine.

Even though galaxies at low redshift are well-fitted by single Sérsic profiles (e.g., Kormendy et al. 2009), this does not necessarily have to be true for galaxies at $z \sim 2$. Therefore, we correct for missing flux using the method described in Szomoru et al. (2010). We find very small deviation in residual-corrected effective radii, with a median absolute deviation of 3.4%. Color images and measured profiles are shown in Figure 3.2.

We repeated the measurements using a variety of PSF stars ($N \sim 25$). We find an absolute median deviation in the half-light radius of $\sim$ 3% for *HST*-WFC3, $\sim$ 3.5% for *HST*-ACS, and $\sim$ 10% for the ground-based UDS-UKIDSS data, due to variations in the PSF. The largest source of uncertainty in the measured profiles is, however, caused by the error in the sky background estimate. Even though these galaxies are among the brightest at this redshift, using the wrong sky value can result in large errors for both $r_{\rm e}$ and n. We determine the error in the sky background estimate by measuring the variations of the residual flux in the profile between 5 and 15 arcsec. For sizes derived from *HST*-ACS, the absolute median deviation in the effective radius due to the uncertainty in background is $\sim$ 13%, and for *HST*-WFC3 $\sim$ 12%. Due to the deeper ground-based UDS-UKIDSS data, the uncertainty for UDS-19627 due to the sky is $\sim$ 8%. All of our results are summarized in Table 3.4.

We note that we find a smaller size and larger n for UDS-19627 as compared to Toft et al. (2012), which cannot be explained within the quoted errors. We have compared our results with the size measurements from Williams et al. (2009) and R. J. Williams (2012, private communication), who also use UDS-UKIDSS data for measuring structural parameters. They too find a smaller size in the K band of $r_{\rm e} = 1.63$ kpc, with a similar axis ratio of $q = 0.53$, while keeping the Sérsic index fixed to $n = 4$. Furthermore, we compare the size of UDS-29410 obtained from the ground-based UDS-UKIDSS data, to the size from *HST*-WFC3 to test how reliable the ground-based data are for measuring structural parameters. From the ground-based UDS H band we find $r_{\rm e} = 1.97 \pm 0.11$ kpc, and $n = 2.47 \pm 0.22$ for UDS-29410 which is consistent with the measurements using the *HST*-WFC3 data within our 1σ errors. From these two independent results, we are confident that our size measurement for UDS-19627 is correct. In what follows, we will use the mean effective radius and Sérsic n from the band which is closest to rest-frame optical r'. The effective radii reported here are circularized, $r_{\rm e} = \sqrt{ab}$.

3.3.4 Dynamical masses

Combining the size and velocity dispersion measurements we are now able to estimate dynamical masses using the following expression:

$$M_{\rm dyn} = \frac{\beta(n)\, \sigma_{\rm e}^2\, r_{\rm e}}{G}. \tag{3.1}$$

Here $\beta(n)$ is an analytic expression as a function of the Sérsic index, as described by Cappellari et al. (2006):

$$\beta(n) = 8.87 - 0.831n + 0.0241n^2. \tag{3.2}$$

This is computed from theoretical predictions for β from spherical isotropic models described by the Sérsic profile, for different values of n, and integrated to one $r_{\rm e}$ (cf. Bertin et al. 2002). The use of a Sérsic-dependent virial constant $\beta(n)$ gives a better correspondence between $M_{\rm dyn}$ and M_* for galaxies in the SDSS (Taylor et al., 2010b). This does require however, that the total stellar masses are also derived using the luminosity of the derived Sérsic profile. Thus we correct our total stellar mass, as derived from the total magnitude as given in the catalogs (measured with Sextractor), to the total magnitude from the Sérsic fit. We note that the values for β that we find are all close to 5, a value often used in the literature (e.g., Cappellari et al. 2006). Our dynamical masses and corrected stellar masses are given in Table 3.4.

3.4 Compilation of kinematic studies

In order to study the structural evolution of quiescent galaxies, we combine the results from different kinematic studies at various redshifts. Where possible, we apply similar corrections as described above.

3.4.1 Low-redshift sample

At low redshift we select galaxies from the SDSS DR7. Stellar masses are based on MPA[1] fits to the photometry following the method of Kauffmann et al. (2003), and Salim et al. (2007). Star formation rates (SFRs) are based on Brinchmann et al. (2004). Structural parameters are from the NYU Value-Added Galaxy Catalog (NYU-VAGC, Blanton et al. 2005). For all galaxies, velocity dispersions were aperture corrected as described in Section 3.3.2, and stellar masses are calculated with a Chabrier (2003) IMF. We furthermore correct the stellar masses using the total magnitude from the best Sérsic fit. All dynamical masses were derived using Equation 3.1. For making an accurate comparison between low- and high-redshift galaxies, we only select non-star-forming galaxies, i.e., sSFR $< 0.3/t_H$ (see Williams et al. 2009), where t_H is the age of the universe at the given redshift.

3.4.2 Intermediate- and high-redshift sample

Our high redshift sample consists of a collection of both optical and NIR spectroscopic studies of individual galaxies. van der Wel et al. (2008) present a sample of quiescent galaxies at $z \sim 1$,

[1] http://www.mpa-garching.mpg.de/SDSS/DR7/

which itself is a compilation of three studies in the following fields: Chandra Deep Field South (CDF-S; van der Wel et al. 2004; 2005), the Hubble Deep Field North (HDF-N; Treu et al. 2005a; 2005b), and cluster galaxies in MS 1054-0321 at $z = 0.831$ (Wuyts et al., 2004). We derive stellar masses for this sample by running the stellar population code FAST on available catalogs, i.e., FIREWORKS (Wuyts et al., 2008) for the CDF-S, R. Skelton et al. (in preparation) for the HDF-N, and FIRES (Förster Schreiber et al., 2006) for MS 1054-0321. For CDF-S and HDF-N the stellar masses are corrected using the total magnitude from the best $n = 4$ fit to be consistent with the structural parameters from van der Wel et al. (2008). For MS 1054-0321, we use structural parameters and stellar mass corrections based on the results by Blakeslee et al. (2006), who fit Sérsic profiles with n as a free parameter. We note that Martinez-Manso et al. (2011) also study a sample of four $z \sim 1$ galaxies, but find dynamical masses that are significantly lower than their stellar masses, in contrast to the result by van der Wel et al. (2008).

Other high-redshift results included here are from Newman et al. (2010) and Bezanson et al. (2013), who use the upgraded red-arm of LRIS on Keck to obtain UV rest-frame spectra of galaxies at $z \sim 1.3$ and $z \sim 1.5$ respectively. Velocity dispersions for two galaxies at $z = 1.41$ are presented by Cappellari et al. (2009), and have been observed with VLT-FORS2 (see also Cenarro & Trujillo 2009). Using NIR spectrographs, Onodera et al. (2012, Subaru-MOIRCS) and van Dokkum et al. (2009, GNIRS) obtained velocity dispersions for two galaxies at $z = 1.82$ and $z = 2.186$. Similar to the current study, Toft et al. (2012) study UDS-19627 using VLT X-Shooter. Dynamical masses were derived using to Equation 3.1. Note that for the studies of Cappellari et al. (2009), Onodera et al. (2012), van Dokkum et al. (2009), and Toft et al. (2012) no stellar mass corrections were applied due to the absence of the necessary information. All structural and kinematic properties of our high-redshift sample are listed in Table 3.4.

3.5 Are stellar masses reliable?

The main goal of this chapter is to see whether the stellar masses at $z \sim 2$ are reliable. Here we compare our stellar masses, as derived from the spectra and photometry, to our dynamical masses, which are derived from effective radii and stellar velocity dispersions (Figure 3.6). Gray squares represent the density of non-star-forming, low-redshift galaxies from the SDSS as described in Section 3.4.1. Other symbols are the high-redshift studies as described in Section 3.4.2. The one-to-one relation for $M_{\rm dyn}$ and M_* is indicated by the dashed line. Note that the region above the line is nonphysical with stellar masses being higher than the dynamical mass.

Most $z > 1.5$ galaxies in this sample are very massive, in the range $11.2 < \log M_{\rm dyn}/M_\odot < 11.8$. At all redshifts, stellar and dynamical masses are tightly correlated and dynamical mass, which includes baryonic and dark matter, is on average higher than stellar mass. Thus, we infer that the stellar masses of our galaxies are broadly correct, and that the apparent size evolution of massive galaxies in photometric studies cannot be explained by errors in the photometric masses (see also van der Wel et al. 2008).

Figure 3.7a shows the ratio of the stellar and dynamical mass as function of redshift for all galaxies with stellar mass $> 10^{11} M_{\odot}$. We see that the average ratio at low-redshift for massive galaxies is a factor of 0.59 with a scatter of 0.12 dex. We note that For MS 1054-0321, the ratio of the stellar to dynamical mass are slightly higher as compared to low redshift galaxies. Up to redshift $z \sim 1.5$ we find a similar value ($\sim$ 0.5) with similar scatter, but at higher redshift, the ratio seems to decline. For galaxies at $z > 1.5$ we find a median ratio of $M_*/M_{\rm dyn} = 0.9$. We quantify the evolution in this ratio by fitting the relation:

$$M_*/M_{\rm dyn} \propto (1+z)^{\alpha}. \qquad (3.3)$$

We use a linear least-squares fit in log-log space using the function $MPFIT$ (Markwardt, 2009), which takes the errors on each individual data point into account. We find a best-fitting value of $\alpha = 0.17 \pm 0.11$, which is shown as the solid black line in Figure 3.7(a). The uncertainty is derived from 1000 bootstrap simulations, where we draw data points randomly from the sample. The quoted error is the standard deviation from the resulting distribution of points. Even though the fit is statistically significant at the $1-\sigma$ level, due to the relatively large measurements errors as compared to low redshift, and the possible selection bias of the high-redshift samples, we are cautious to draw any strong conclusions from this result.

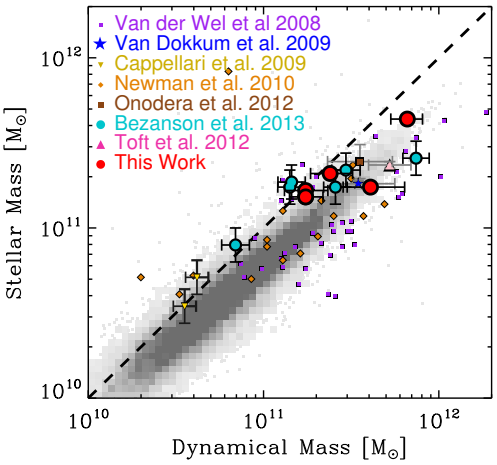

Figure 3.6: Comparison of the stellar mass vs. the dynamical mass. Gray squares are non-star-forming galaxies from the SDSS. Different symbols are from a compilation of high-redshift galaxies as described in Section 3.4.2. The dashed line is for equal dynamical and stellar mass. Low-redshift galaxies are all below the line, as is expected given the contribution of dark matter. All our high-redshift galaxies have dynamical masses that are close to the stellar mass. This suggests that the stellar mass measurements at high-redshift are robust for passive galaxies.

It is tempting to speculate that the evolution in $M_*/M_{\rm dyn}$ might have been caused by a decrease in the dark matter fraction as a function of redshift. For galaxies growing in size over time, the dark matter fraction within $r_{\rm e}$ will also increase. As the dark matter profile is less steep than the stellar mass profile, the dark matter to stellar mass fraction increases with radius, in a similar fashion as shown here (e.g., Hopkins et al. 2009). If so, this could also indicate that the IMF at high-redshift is very similar to the IMF at low-redshift.

Figure 3.7(b) shows $M_*/M_{\rm dyn}$ vs. the evolution of the effective radius at fixed dynamical mass (see Section 3.6.2 and Figure 3.9). Although there is significant scatter, we do find the galaxies with high $M_*/M_{\rm dyn}$ also tend to have smallest size at fixed dynamical mass. Galaxies that are closest to the present-day mass-size relation (dashed vertical line) show lower ratios of stellar to dynamical mass.

We test this claim by using the the following equation:

$$M_*/M_{\rm dyn} \propto \left(r_{\rm e}(z) \,/\, r_{\rm e}(z \sim 0.1)\right)^{\alpha}. \qquad (3.4)$$

We find $\alpha = -0.16 \pm 0.10$, where the error is determined in a similar way as described for Equation 3.3 using the bootstrap method. Furthermore, we use the Spearman's rank test on

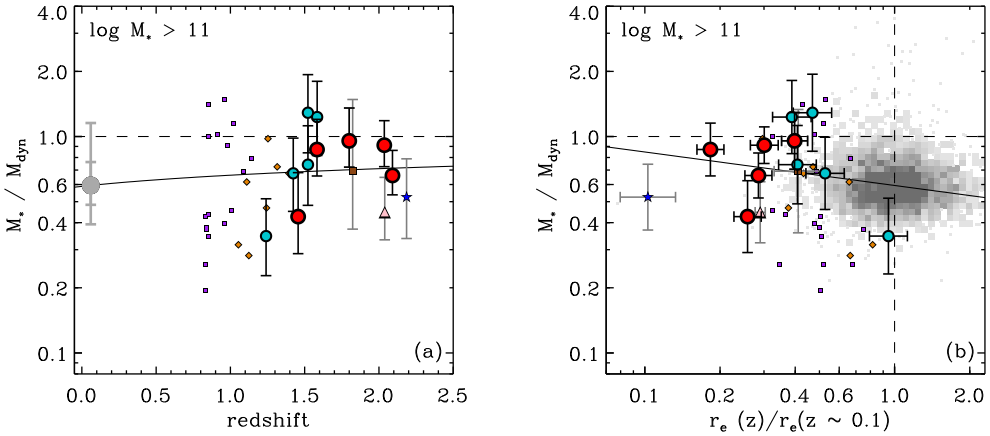

Figure 3.7: (a) Stellar mass divided by the dynamical mass vs. redshift. Galaxies below the line have dynamical mass greater than the stellar mass, above the line is the non-physical regime. For SDSS galaxies with stellar mass $> 10^{11} M_{\odot}$, we find that they have a median $M_*/M_{\rm dyn}$ of 0.59. Up to redshift $z = 1.5$ we find a similar slightly lower median value (~ 0.5), but it rapidly increases at $z > 1.5$ with median a of $M_*/M_{\rm dyn} = 0.9$. The solid line is the best-fit $M_*/M_{\rm dyn} \propto (1+z)^{0.17\pm0.11}$. We caution that this result might be biased due to the selection effects as explained in Section 3.3, and relatively large measurement errors. (b) Stellar mass divided by the dynamical mass vs. the evolution in the effective radius at fixed dynamical mass. Galaxies which have small effective radii at fixed dynamical mass also show higher ratios of $M_*/M_{\rm dyn}$, although there is a significant scatter. The solid line is the best-fit $M_*/M_{\rm dyn} \propto (r_{\rm e}(z) \,/\, r_{\rm e}(z \sim 0.1))^{0.16\pm0.10}$.

the intermediate- and high-redshift data. This confirms that there is an anti-correlation with a probability of 96%. The best-fitting Spearman's rank correlation coefficient is -0.28 ± 0.08. Even though we find a weak anti-correlation, this agrees with the idea that the decreasing ratio of $M_*/M_{\rm dyn}$ with time might be correlated to the size growth of massive galaxies.

3.6 Structural evolution of quiescent galaxies

In this section, we will re-examine the structural evolution of massive quiescent galaxies but now using dynamical measurements.

3.6.1 Bias towards compact galaxies

As noted in Section 3.2.1, this sample is biased towards young quiescent galaxies. Therefore, we will first investigate whether our sample and that of Bezanson et al. (2013) are biased in size as compared to other high-redshift galaxies. We gathered structural properties of galaxies from two studies that use CANDELS data in the UDS and GOODS-South fields (Patel et al. 2012; Szomoru et al. 2012). We compare to a subsample of these galaxies that are determined to be quiescent from their rest-frame U-V and V-J colors (see e.g., Figure 3.1(a)). When comparing the effective radii vs. the stellar mass in Figure 3.8(a), we find that our galaxies (red circles) and those of Bezanson et al. (2013, cyan circles) are in general more compact as compared to the high-redshift CANDELS galaxies (small green circles).

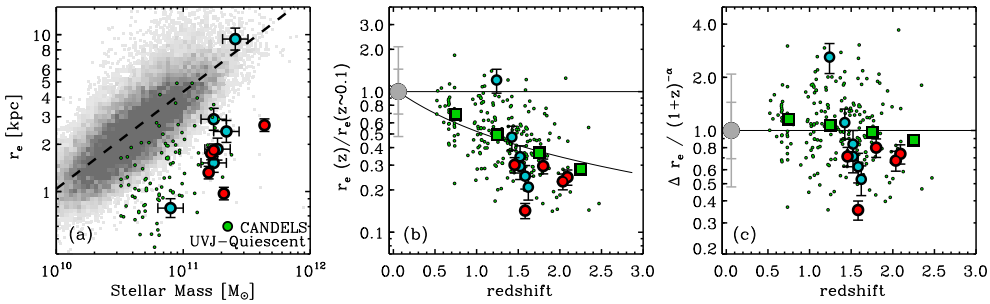

Figure 3.8: Structural comparison of our spectroscopic sample to the full quiescent galaxy population. (a) Effective radii vs. mass for low- and high-redshift galaxies. Gray squares are non-star-forming $z \sim 0$ galaxies from the SDSS, with the dashed line the best-fit to Equation 3.5. High-redshift quiescent galaxies ($1.4 < z < 2.1$) from CANDELS (Grogin et al. 2011; Koekemoer et al. 2011) are shown as small green circles, together with our spectroscopic sample shown as red circles, and the sample by Bezanson et al. (2013) shown as cyan circles. At fixed mass, our high-redshift galaxies have smaller effective radii, similar to what has been found by many studies. (b) Evolution in effective radius at fixed stellar mass, thus corrected for the $M_* - r_e$ relation in panel (a). Big green squares are the median effective radii in bins of redshift for the CANDELS data. The solid line is the best-fit $r_e \propto (1+z)^{-1.02\pm0.05}$. At similar redshift, we find that our sample and that of Bezanson et al. (2013) are mostly below this fit, indicating that our samples our biased towards smaller effective radii. (c) Similar to the panel (b), but now divided by $(1+z)^{-1.02}$ for a better comparison of our spectroscopic sample to the CANDELS data. When comparing the median of our sample to the binned median of other quiescent galaxies at similar redshift, we find smaller effective radii by a factor ~ 1.28. This might be explained by our selection which is based on aperture magnitude, which tends to be biased towards smaller galaxies.

For low-redshift galaxies we parametrize the mass-size relation by:

$$r_e = r_c \left(\frac{M_*}{10^{11} M_\odot} \right)^b \tag{3.5}$$

(Shen et al. 2003; van der Wel et al. 2008). Using a linear least-squares fit in log-log space, we find best fitting values of $r_c = 4.32$ kpc and $b = 0.62$. This is slightly different from the fit by Shen et al. (2003) who find $r_c = 4.16$ kpc and $b = 0.56$. The difference may be explained by different selection criteria, and their use of an older release version of SDSS. Figure 3.8(b) shows the evolution in effective radius, by comparing galaxies with similar mass at different redshifts. Using both the SDSS and the CANDELS data, we examine the amount of evolution in size by fitting the following relation:

$$r_e \propto (1+z)^\alpha, \tag{3.6}$$

We find $\alpha = -1.02 \pm 0.05$ (linear fit in log-log space). Our spectroscopic targets and those of Bezanson et al. (2013) are mostly below this best-fit relation, being smaller by a factor of ~ 1.28 as compared to median in redshift bins (big green squares). This is especially clear from Figure 3.8(c), where we correct for the evolution in size.

This bias might be explained by the method our targets are selected. As our selection is based on the magnitude within a fixed aperture of $1\farcs5$, instead of the total magnitude, we create a bias towards compact galaxies. For galaxies with similar total magnitudes, the smaller galaxies will be brighter within a photometric aperture, and thus make it into our sample.

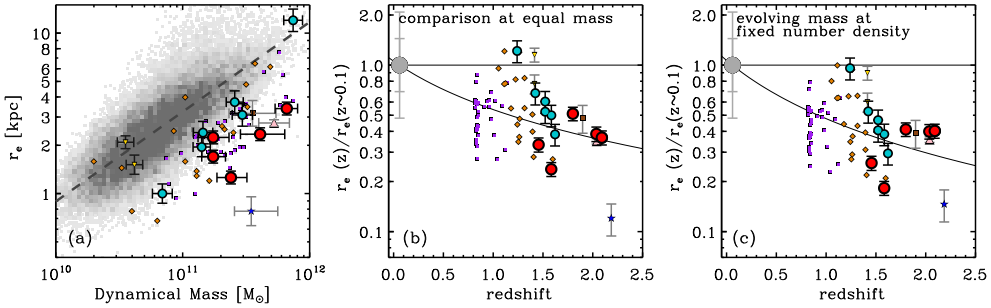

Figure 3.9: Redshift evolution of the effective radius of passive galaxies. (a) Size vs. dynamical mass. The dashed line is the best-fit derived using Equation 3.7 for non-star-forming SDSS galaxies. At fixed dynamical mass, we find that $z \sim 2$ galaxies (red circles) are smaller by a factor ~ 3 compared to low-redshift galaxies. (b) Evolution of the effective radius at fixed dynamical mass vs. redshift. The solid line is the best-fit $r_e \propto (1+z)^{-0.97\pm0.1}$, similar to what has been found by other stellar kinematic studies at high-redshift. Similar to Figure 3.8, our sample is below the best-fit line to the entire high-redshift sample. (c) Evolution of the effective radius using an evolving mass function at constant number density. We now compare galaxies at high-redshift, to more massive galaxies at low-redshift, assuming the mass evolves as $\Delta \log M/M_\odot \sim 0.15z$. This time, we find an even stronger evolution, with $r_e \propto (1+z)^{-1.16\pm0.1}$.

In what follows, we correct for this bias by increasing our sizes and those of Bezanson et al. (2013) by a factor of 1.28, and decreasing the velocity dispersion by a factor of $\sqrt{1.28}$.

3.6.2 Evolution in size

In Figure 3.9(a) we plot effective radius vs. dynamical mass. Symbols are the same as in Figure 3.7. For the low-redshift galaxies we parametrize the mass-size relation according to the following equation

$$r_e = r_c \left(\frac{M_{\rm dyn}}{10^{11} M_\odot} \right)^b, \tag{3.7}$$

and find $r_c = 3.23$ kpc and $b = 0.56$ (dashed line). This is in good agreement with $b = 0.56$ and $r_c = 3.26$ kpc as found by van der Wel et al. (2008). At fixed dynamical mass, we see that all our galaxies have smaller effective radii as compared to low-redshift. This finding is further illustrated in Figure 3.9(b), where we compare the effective radii at fixed dynamical mass to the mass-size relation at $z \sim 0$. The solid line is the best-fit as described by equation 3.6, with $\alpha = -0.97 \pm 0.1$. This result is in agreement to with what has been found in previous kinematical studies (van der Wel et al. 2008; Newman et al. 2010). The scatter between different studies is considerable, with the work by van Dokkum et al. (2009) having the largest size difference while that by Onodera et al. (2012) having the smallest. Our sample falls in between these two extremes, i.e., we find smaller sizes as compared to Onodera et al. (2012), but larger effective radii than van Dokkum et al. (2009).

Instead of comparing galaxies sizes at fixed dynamical mass, we will now take into account that galaxies do grow in mass (e.g., Patel et al. 2012). In van Dokkum et al. (2010) they find that, for a sample selected at a constant number density, the stellar mass evolves as

$$log M_n/M_\odot = 11.45 - 0.15z. \tag{3.8}$$

The number density on which this result is based, $n = 2 \times 10^{-4}\mathrm{Mpc}^{-3}$, corresponds to an average mass of $\log M_*/M_\odot \sim 11.2$ at $z \sim 2$, similar to our sample. Assuming that the mass evolves as $\Delta \log M/M_\odot \sim 0.15z$, we will compare effective radii for galaxies at different redshifts. For example, a galaxy with $\log M_{\rm dyn}/M_\odot = 11$ at $z \sim 2$ will be compared with a $z \sim 0$ galaxy with $\log M_{\rm dyn}/M_\odot = 11.3$.

However, the evolution in stellar mass is determined for a complete sample of both star forming and quiescent galaxies, while in this chapter we only look at quiescent galaxies. Therefore, we assess whether the evolution in size at constant cumulative number density is different for the quiescent population as compared to the full population. This was already done for galaxies in CANDELS by Patel et al. (2012) at $n_{cum} = 1.4 \times 10^{-4}\mathrm{Mpc}^{-3}$, which corresponds to a median mass of $\log M_*/M_\odot \sim 10.9$ at $z \sim 1.8$. The sample studied here, however, has a median mass of $\log M_*/M_\odot \sim 11.2$ at $z \sim 1.8$, which corresponds to $n_{cum} = 2.5 \times 10^{-5}\mathrm{Mpc}^{-3}$. Thus, we repeat the analysis by Patel et al. (2012), but now using our CANDELS sample (Section 3.6.1) at this lower constant cumulative number density. Our results are similar to Patel et al. (2012), i.e., the quiescent population has smaller effective radii as compared to full population, but the difference in size between the quiescent and star-forming population is slightly smaller at $z < 1.8$ as compared to Patel et al. (2012). The difference is due to the fact that at our lower constant cumulative number density, we find a higher fraction of quiescent galaxies. Therefore, the effective radii of the full population will be closer to the effective radii of the quiescent population, as compared to Patel et al. (2012). To correct for this difference in size, we increase the effective radii of all the quiescent galaxies in our combined sample by the size difference of the quiescent population as compared to the full. We correct each galaxy individually by finding the correction factor at this particular redshift. Below $z < 1.8$, the median correction factor is ~ 1.05, while at $z \sim 2.1$ the correction factor is ~ 1.6.

Figure 3.9(c) shows the evolution in size at fixed number density as a function of redshift. Not surprisingly, the evolution in effective radii is more extreme, as we are now comparing $z \sim 2$ galaxies to more massive, and therefore bigger galaxies at $z \sim 0$. Using Equation 3.6, we find that $\alpha = -1.16 \pm 0.1$ provides the best fit. In conclusion, assuming that galaxies evolve in both mass and size, we find that the effective radii have to grow by a factor ~ 4 from $z \sim 2$ to the present day.

3.6.3 Evolution in velocity dispersion

In Figure 3.10(a) we compare the stellar velocity dispersion within one $r_{\rm e}$ vs. the dynamical mass for both low- and high-redshift samples. The dashed line is the parametrization of the $\sigma_{\rm e} - M_{\rm dyn}$ relation for low$-z$ galaxies using the following equation:

$$\sigma_{\rm e} = \sigma_c \left(\frac{M_{\rm dyn}}{10^{11} M_\odot} \right)^b . \tag{3.9}$$

We find that $\sigma_c = 148.9\ \mathrm{km\ s}^{-1}$ and $b = 0.24$. Our high-redshift sample is clearly offset from low-redshift galaxies in the SDSS, i.e., at fixed mass they have higher velocity dispersions. Comparison of the velocity dispersion at fixed dynamical mass, as seen in 3.10b, shows a clear evolution in $\sigma_{\rm e}$, such that velocity dispersion decreases over time. From this figure the

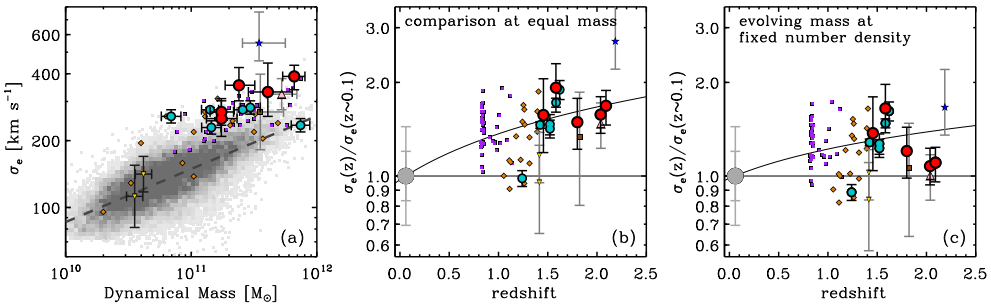

Figure 3.10: Redshift evolution in stellar velocity dispersion within one effective radius (σ_e). (a) σ_e vs. dynamical mass. At fixed dynamical mass, we find that our galaxies have higher velocity dispersion as compared to low-redshift galaxies. (b) Evolution of velocity dispersions at fixed dynamical mass vs. redshift. We find the $\sigma_e \propto (1+z)^{0.49\pm0.08}$, i.e., at fixed dynamical mass the velocity dispersion decreases by a factor of ~ 1.7 from $z \sim 2$ to the present day. (c) Evolution of the velocity dispersion for an evolving mass function at constant number density. Opposite to the evolution in size, we now find a milder evolution of $\sigma_e \propto (1+z)^{0.31\pm0.08}$.

increase in accuracy for the velocity dispersion measurements of this study, as compared to other studies at similar redshift, is also clearly noticeable. Again we use the following simple relation to quantify the amount of evolution:

$$\sigma_e \propto (1+z)^{\alpha}, \tag{3.10}$$

and find that $\alpha = 0.49 \pm 0.08$. From $z \sim 2$ to $z \sim 0$ the stellar velocity dispersions decrease by a factor ~ 1.7. Again, we note that we apply a correction to the velocity dispersions in our sample, in order to correct for the bias towards more compact galaxies (section 3.6.1).

If we now compare low- and high-redshift galaxies using an evolving mass function as described above, we find that the velocity dispersion decreases less with cosmic time than when compared at fixed dynamical mass. Here, we also take into account that quiescent galaxies at constant cumulative number density are smaller as compared to the full sample, and therefore they have higher velocity dispersions. Similar to as described above, we therefore corrected the velocity dispersions of all galaxies in our combined sample. At $z < 1.8$, velocity dispersions on average decrease by a factor of $\sim \sqrt{1.05}$, while at $z \sim 2.1$ they decrease by a factor of $\sim \sqrt{1.6}$. If we use equation 3.10, we find that $\alpha = 0.31 \pm 0.08$. In other words, the velocity dispersion within one r_e decreases by a factor ~ 1.4 from $z \sim 2$ to present-day.

3.6.4 Evolution in mass density

Next, we will focus on the central and effective mass densities using a similar approach as described in Saracco et al. (2012). In short, using the intrinsic Sérsic profile we can calculate the fraction of the luminosity that is within 1 kpc as compared to the total luminosity. For a Sérsic profile this ratio is given by (Ciotti, 1991):

$$\frac{L_{1\mathrm{kpc}}}{L_{\mathrm{tot}}} = \frac{\gamma(2n,x)}{\Gamma(2n)}. \tag{3.11}$$

Here, $\Gamma(2n)$ is the complete gamma function, $\gamma(2n,x)$ the incomplete gamma function, $x = b_n(r_{1\mathrm{kpc}}/r_e)^{1/n}$, with $b_n = 1.9992n - 0.3271$. Using this ratio we can now calculate the

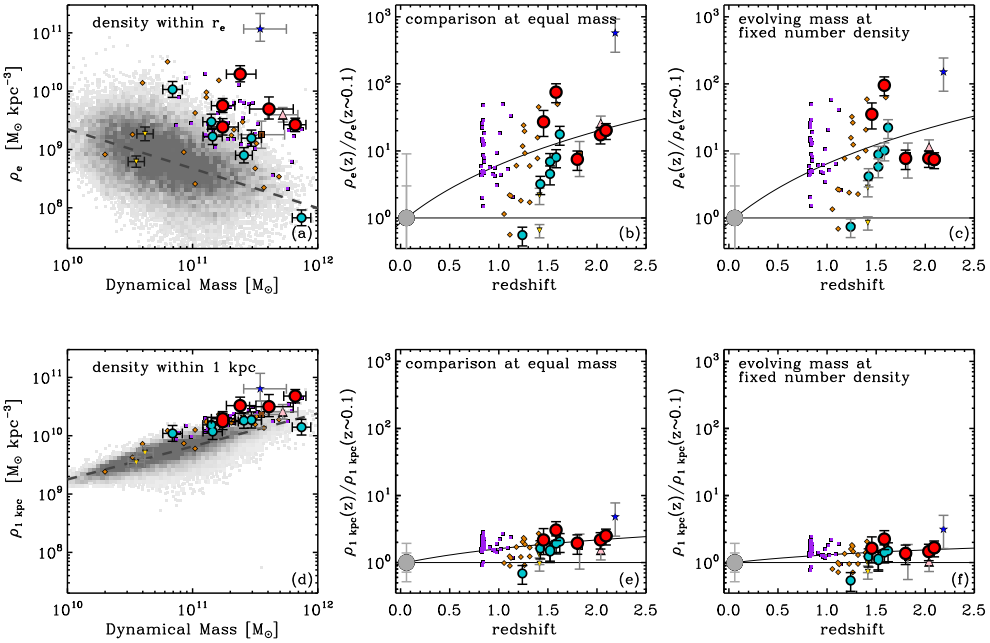

Figure 3.11: Redshift evolution of the central and effective densities, as calculated according to Equations 3.13 and 3.14. Top row shows the results for the effective mass density, while the bottom row shows the mass density within 1 kpc. *Left panels:* the density within r_e vs. dynamical mass (a). We find that low-redshift galaxies show a large scatter at fixed dynamical mass. Still, our high-redshift galaxies have higher densities within r_e at fixed mass. In contrast to ρ_e, the density within 1 kpc vs. dynamical mass (d) shows very little scatter, and we find only a small difference between low- and high-redshift galaxies. *Middle panels:* evolution in the density at fixed dynamical mass vs. redshift. We find a strong evolution for the effective density (b) with $\rho_e \propto (1+z)^{2.86\pm0.15}$, or a decrease by a factor of ~ 2 from high-redshift to $z \sim 0$. For the central density, however, we only find that $\rho_{1kpc} \propto (1+z)^{0.74\pm0.15}$, or a decrease of ~ 2.3. *Right panels:* evolution of the density with an evolving mass at constant number density. Similar to the effective radii, we find a stronger evolution for the effective density, i.e., $\rho_e \propto (1+z)^{2.93\pm0.15}$, while the central density requires very little to no evolution ($\rho_{1kpc} \propto (1+z)^{0.42\pm0.15}$).

dynamical mass within one 1 kpc and within r_e from the total mass:

$$M_{1\mathrm{kpc}} = \frac{L_{1\mathrm{kpc}}}{L_{\mathrm{tot}}} M_{\mathrm{dyn}}. \tag{3.12}$$

Here we assume that the dynamical mass profile follows the light profile, and furthermore that the mass-to-light ratio of the galaxy is radially constant. The detection of small color gradients in our galaxies indicates, however, that this is not the case, but the effect on the derived densities is small (Saracco et al. 2012; see also Szomoru et al. 2012). Finally, the densities are calculated as follows:

$$\rho_{1\mathrm{kpc}} = \frac{M_{1\mathrm{kpc}}}{4/3\pi r_{1\mathrm{kpc}}^3}, \tag{3.13}$$

and

$$\rho_e = \frac{0.5 M_{\rm dyn}}{4/3\pi r_{\rm e}^3}. \tag{3.14}$$

As for $r_{\rm e}$ and $\sigma_{\rm e}$, we now compare the density as a function of dynamical mass (see Figure 3.11). The top row shows the results for the mass density within one effective radius, while the bottom row compares the central density within 1 kpc. The first thing to notice is the large scatter for low-redshift galaxies when looking at ρ_e vs. $M_{\rm dyn}$, while $\rho_{\rm 1kpc}$ vs. $M_{\rm dyn}$ shows a tight relation. The density-mass relation can be parametrized by:

$$\rho = \rho_c \left(\frac{M_{\rm dyn}}{10^{11} M_\odot} \right)^b. \tag{3.15}$$

For the density within $r_{\rm e}$ we find $\rho_{c,e} = 4.7 \times 10^8 M_\odot {\rm kpc}^{-3}$ and $b_e = -0.68 \pm 0.15$, and for the central density within 1 kpc $\rho_{c,1kpc} = 6.6 \times 10^9 M_\odot {\rm kpc}^{-3}$ and $b_{\rm 1kpc} = 0.56$.

When we compare the galaxies in our high-redshift sample to galaxies in the SDSS, we find that they have higher densities within $r_{\rm e}$. Comparison at equal dynamical mass shows that the effective densities are higher by a factor of ~ 50 (Figure 3.11(b)) for our sample. The same comparison, but now for the central density within 1 kpc, reveals only mild evolution, approximately a factor of ~ 3 from $z \sim 2$ to the present. When fitting

$$\rho \propto (1+z)^\alpha, \tag{3.16}$$

we find that $\alpha_e = 2.86 \pm 0.15$, while $\alpha_{\rm 1kpc} = 0.74 \pm 0.15$.

Instead of comparing galaxies at fixed mass, we again take into consideration that galaxies evolve in mass when comparing low- and high-redshift galaxies. Again, we correct for the fact that quiescent galaxies at constant cumulative number density are smaller as compared to the full sample. This time, we find that ρ_e evolves even faster as compared to the equal mass comparison $\alpha_e = 2.93 \pm 0.15$. The density within 1 kpc, however, requires a decrease less than a factor of ~ 2, with $\alpha_{\rm 1kpc} = 0.42 \pm 0.15$, from $z \sim 2$ to the present

3.7 Discussion

In the previous section we have found that in order for the high-redshift galaxies in our sample to evolve into typical present-day early-type galaxies, strong structural evolution is required. Effective radii need to increase, and the velocity dispersion within $r_{\rm e}$ has to decrease. The density within the effective radius has to decrease by more than an order of magnitude. However, the central density can remain almost the same, consistent with inside-out growth.

The dominant physical mechanism for this structural evolution is still a subject of ongoing debate. Size growth dominated by major mergers seems to be unlikely as it would increase the masses too much, which would make extremely massive galaxies too common in the local universe. As the mass and size increase at approximately at the same rate in major mergers, the galaxies would also remain too compact for their mass. Minor merging could offer a solution to the problem, as it can grow a galaxy in effective radius ($r_{\rm e}$) steeper than $r_{\rm e} \propto M_*$ (Villumsen 1983; Naab et al. 2009; Bezanson et al. 2009; Hopkins et al. 2009b). In this scenario, the observed compact high-redshift galaxies may simply be the cores of local massive early-type

galaxies, which grow inside-out by accreting (smaller) galaxies, and thus assemble a significant part of their mass at later times (van der Wel et al. 2009; Oser et al. 2010). In this section we will examine whether dry minor merging agrees with our findings.

From a simple estimate, based on the virial theorem, Bezanson et al. (2009) predict how the effective radii changes if a massive galaxy undergoes a series of minor mergers. With only eight 1:10 mergers, the effective radii can grow by a factor of ~ 5 while only having the mass increase by a factor of $\sim$ 2. This is also described by Naab et al. (2009), who state that if an initial system undergoes a mass increase by a factor of 2 due to accretion of very small systems, then the final radius of the system is four times larger, the velocity dispersion is reduced by a factor of 2, and the density is reduced by a factor of 32. This analytic prediction is confirmed by their hydrodynamical cosmological simulation and consistent with the observational size evolution as presented here.

Using hydrodynamic simulations of galaxy mergers, Hopkins et al. (2009), also find evidence for size evolution. When they compare the effective radii of quiescent galaxies at fixed mass, they find an evolution in size of $r_{\rm e} \propto (1+z)^{-0.48}$ for galaxies with $\log M_*/M_\odot = 11$, which is weaker than found by this study and many others. Oser et al. (2012) find a size evolution in their hydro simulation, which is much stronger: $r_{\rm e} \propto (1+z)^{-1.44}$, on the high side of current observational results.

Oser et al. (2012) find a similar evolution in velocity dispersion of $\sigma \propto (1+z)^{0.44}$, to that found in this work. In contrast, Hopkins et al. (2009), predict that high-redshift quiescent galaxies have roughly the same or at most a factor ~ 1.25 larger velocity dispersions.

Evolution of the density is also discussed in both Bezanson et al. (2009) and Hopkins et al. (2009b). Based on photometric data, both studies find that while the density within one effective radius is higher at high-redshift, the central density of high-redshift galaxies is very similar to local massive ellipticals. From hydro simulations, Naab et al. (2009) show that the central density within 1kpc decreases by a factor of 1.5 from $z = 2$ to $z = 0$, caused by dynamical friction from the surviving cores of the infalling systems. Similarly, Oser et al. (2012) show that the central density evolves only weakly, while the density within $r_{\rm e}$ decreases rapidly by more than an order of magnitude, in good agreement with what we find here. From a study of central galaxies in three $\sim 10^{13}\,M_\odot$ galaxy groups, simulated at high resolution in cosmological hydrodynamical simulations, Feldmann et al. (2010) come to the same conclusion. They find that the effective density of these galaxies decreases by 1-2 orders of magnitude between $z = 1.5$ and $z = 0$, while the density within 2 kpc stays roughly constant.

This is in contrast with the findings of Saracco et al. (2012), who find no evidence for higher mass densities within one effective radius when comparing their $z \sim 1.5$ galaxies to low-redshift cluster galaxies. Furthermore, the large scatter that they observed in the effective density and the apparent evolution, is simply due a peculiar analytic feature in the Sérsic profile.

In Figure 3.7(a) we show that the ratio of $M_*/M_{\rm dyn}$ appears to have evolved from $z \sim 2$ to $z \sim 0$. As compared to SDSS galaxies with $\log M_*/M_\odot > 11$, we find that the median $M_*/M_{\rm dyn}$ is higher by 50% at $z > 1.5$, and that $M_*/M_{\rm dyn} \propto (1+z)^{0.17\pm0.011}$. However, this result is uncertain due to the selection effects inherent in this sample and large measurement errors in both masses. We note that this effect is predicted by simulations; as the effective radius of a galaxy grows, the dark matter fraction within $r_{\rm e}$ will also increase. Hopkins et al. (2009) predicts evolution by a factor of ~ 1.25 for galaxies with $\log M_*/M_\odot = 11$, with the

effect increasing with stellar mass. Hilz et al. (2012) also find a strong evolution in the dark matter fraction in their hydro-simulation, and predict that quiescent galaxies at $z \sim 2$ have lower dark matter fractions (80%). They mention that it is mainly driven by the strong size increase, which therefore probes a larger region that is dominated by dark matter.

3.8 Summary and conclusion

In this chapter, we present deep UV-NIR spectroscopy of five massive ($> 10^{11}\ M_{\odot}$) galaxies at $z \sim 2$, using X-Shooter on the VLT. These spectra enable us to measure stellar velocity dispersions with higher accuracy than done before at this redshift: we triple the sample of $z > 1.5$ galaxies with well constrained ($\delta\sigma < 100$ km s^{-1}) velocity dispersion measurements. We find that the stellar velocity dispersions are high (290-450 km s^{-1}) compared to equal-mass galaxies in the SDSS.

We combine these kinematic results with size measurements using GALFIT on *HST*-WFC3 H_{160} and UDS K-band imaging, and use these measurements to derive dynamical masses. Stellar masses are obtained from SPS modeling on the VIS-NIR spectra in combination with the available broadband and medium-band data. The SPS-modeling shows that our galaxies have ages ranging from 0.5 to 2 Gyr, and show no signs of on-going star formation.

We find good correspondence between the dynamical and stellar masses, with the dynamical mass being higher by $\sim 15\%$. Our results suggest that stellar mass measurements for quiescent galaxies at high-redshift are robust.

We complement our results with stellar kinematic results from other studies at low and high redshift to study the structural evolution of massive quiescent galaxies. At fixed dynamical mass, we find that the effective radius increases by a factor of ~ 2.8, while the velocity dispersion decreases by a factor of ~ 1.7 from $z \sim 2$ to the present day. Furthermore, we study how the mass density within $r_{\rm e}$ and 1 kpc evolves with time. We find a strong decrease of the mass density within one effective radius (factor of ~ 21), while it only decreases mildly within 1 kpc (factor of ~ 2.3). Instead of comparing galaxies at fixed dynamical mass, we also use an evolving mass limit as defined by fixed number density. By accounting for concurrent mass growth in our comparison of high- and low-redshift galaxy populations, we find an even stronger evolution in galaxy sizes (factor of ~ 4). We find that velocity dispersion decreases less dramatically with time, differing by only a factor of ~ 1.4 between $z \sim 2$ and $z \sim 0$. Finally, for the mass density within $r_{\rm e}$, we find a stronger evolution, but interestingly, the mass density within 1 kpc is consistent with no evolution. This finding implies that massive quiescent galaxies grow inside out.

We examine if our results are compatible with the current idea of inside-out growth through dry minor mergers. Our findings are qualitatively consistent with predictions from hydrodynamical simulations which show similar evolution in size, velocity dispersion, and mass density within one effective radius.

Finally, we find that even though the stellar masses are consistent with the dynamical masses, the ratio of $M_*/M_{\rm dyn}$ may slightly decrease with time. This, too, is predicted by minor merging simulations, which show that the size growth due to minor merging will also change the fraction of dark matter as compared to the stellar mass within an effective radius. This is due to the fact that the dark matter profile is less steep than the stellar mass profile, and thus

the dark matter to stellar mass fraction increases with radius.

Despite the vastly improved accuracy of our derived dynamical masses and stellar population parameters, the broader inferences of our study are still limited by the small number of high-redshift galaxies with such information. We have shown that our sample is biased towards younger galaxies, compared to a stellar mass limited sample at $z \sim 2$, with smaller effective radii as compared to the full population of quiescent galaxies at $z \sim 2$. Only with a larger unbiased sample of massive quiescent galaxies at high redshift can we start to comprehend the final phase that massive galaxies go through in becoming today's ellipticals.

Acknowledgments

We thank Daniel Szomoru for providing his residual-correct code and the galaxy sizes for GOODS-S CANDELS; Andrew Newman for providing the corrected stellar masses; Shannon Patel for the structural parameters of galaxies in UDS CANDELS; and Ivo Labbé for helpful comments regarding the SFRs from 24 flux. It is a pleasure to acknowledge the contribution to this work by the NMBS collaboration. We also thank Adam Muzzin for useful discussions.
This research was supported by grants from the Netherlands Foundation for Research (NWO), the Leids Kerkhoven-Bosscha Fonds. Support for the program *HST*-GO-12167.1 was provided by NASA through a grant from the Space Telescope Science Institute.
This work is based on observations taken by the CANDELS Multi-Cycle Treasury Program with the NASA/ESA *HST*, which is operated by the Association of Universities for Research in Astronomy, Inc., under NASA contract NAS5-26555.
This publication also makes use of the Sloan Digital Sky Survey (SDSS). Funding for the creation and distribution of the SDSS Archive has been provided by the Alfred P. Sloan Foundation, the Participating Institutions, the National Aeronautics and Space Administration, the National Science Foundation, the U.S. Department of Energy, the Japanese Monbukagakusho, and the Max Planck Society. The SDSS Web site is http://www.sdss.org/. The SDSS Participating Institutions are the University of Chicago, Fermilab, the Institute for Advanced Study, the Japan Participation Group, Johns Hopkins University, the Max Planck Institut fur Astronomie, the Max Planck Institut fur Astrophysik, New Mexico State University, Princeton University, the United States Naval Observatory, and the University of Washington.

3.A Robustness of the velocity dispersion measurements

As it has only recently become possible to measure velocity dispersions at high redshift, the stability of these measurements has barely been tested. In this appendix, we will study the effect of fitted wavelength range, template choice, degree of the additive polynomial, S/N of the spectra, and the choice of stellar populations models.

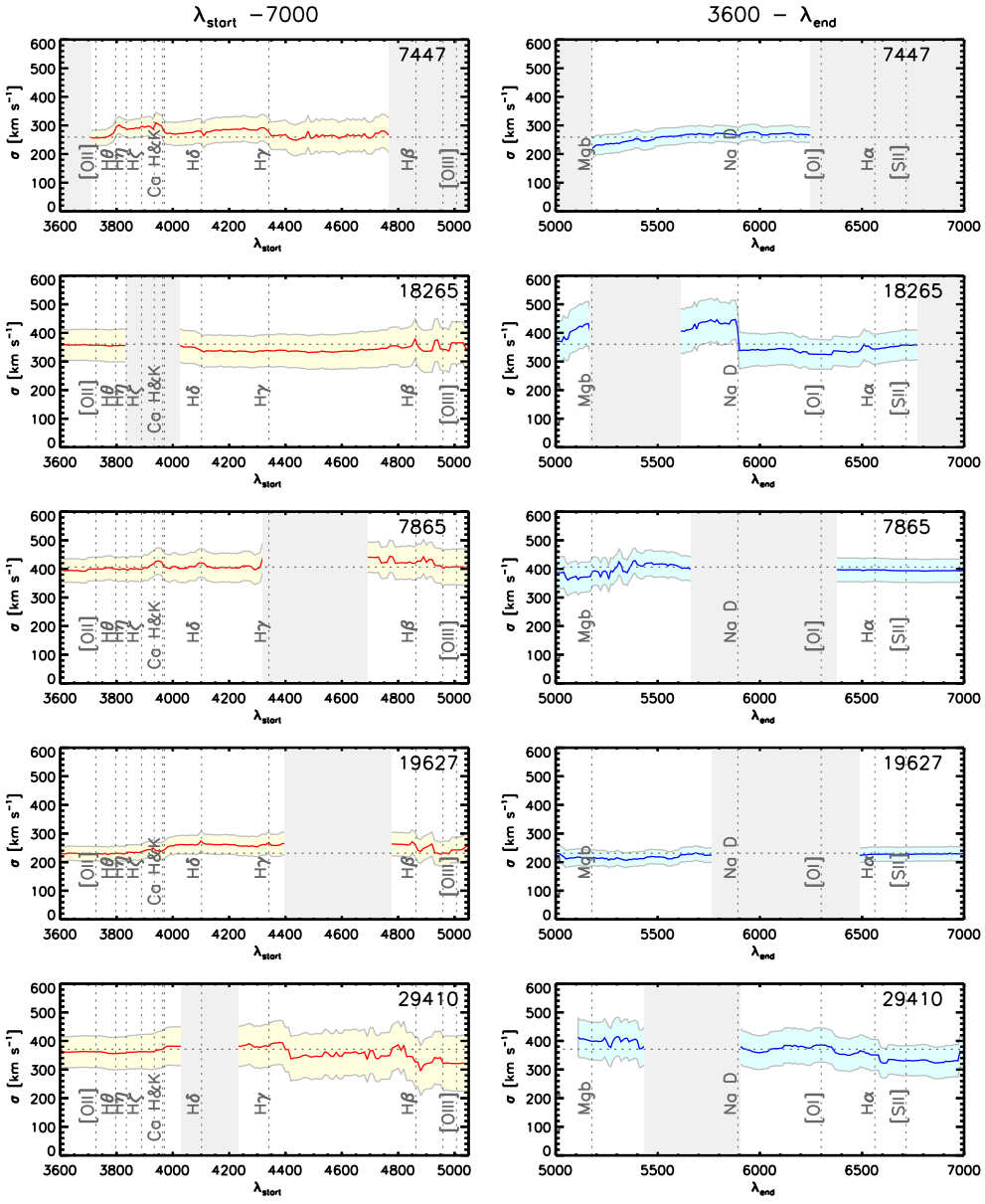

Figure 3.12: Velocity dispersion vs. wavelength range. Left panel shows the results for $\lambda_{\rm start} < \lambda < 7000$ Å, while the right panel is for 3600 Å$< \lambda < \lambda_{\rm end}$. The horizontal shaded region indicates the 1-σ error from pPXF, and the dashed horizontal line indicates the velocity dispersion when fitting the full range. Most prominent absorption lines are indicated, and the regions affected by strong sky-lines and atmospheric absorption are shown in gray. Overall, we find a stable solution for the velocity dispersion while changing the wavelength range. For NMBS-C7447 and UDS-19627, we do find a small increase in the region around the Balmer break. For NMBS-C18265, we find that excluding Na D has a great impact on the velocity dispersion.

3.A.1 Dependence of the velocity dispersion on the wavelength range

Our sample spans a redshift range of $1.4 < z < 2.1$, which means that different parts of the rest-frame spectra will be affected by sky-lines and atmospheric absorption for each galaxy. This can be seen from Figure 3.4, we often lose strong absorption features in our spectrum, which affects the region of the rest-frame spectrum that we can fit. Here we investigate how stable the measured velocity dispersion is as a function of the wavelength range.

For the velocity dispersion fitting in this chapter, the lower wavelength limit is set by stellar libraries and models, as no systematic high-resolution observations exist below 3550 Å. The higher wavelength limit is set by lower S/N in our spectra in the observed K-Band. Our approach for testing the wavelength dependence of the fit is as follows. First, we use the full-range spectrum to determine a best-fit polynomial (1 order per 10 000 km s^{-1}), which is used to correct for the difference between the observed and the template continuum. Next, we repeat the measurement with a zeroth-order polynomial while changing the start or end wavelength. The polynomial is not a free parameter in this fit, as this would make it impossible to separate between the effect of the polynomial and the wavelength range. Note also, that we use a single template for all fits as determined from the full Visual+NIR spectrum together with broadband and medium-band data (see Section 3.3.1).

Figure 3.12 shows the results for the different sources. The left panel shows the result where we change the starting wavelength, i.e., the wavelength range is $\lambda_{\rm start} < \lambda < 7000$ Å, whereas the panels on the right show the effect of changing the end wavelength, 3600 Å$< \lambda < \lambda_{\rm end}$. The first thing to notice is that the measured dispersions are remarkably stable, even when most of the absorption lines have been excluded from the fit. The two galaxies with the youngest ages and strong Balmer absorption lines (NMBS-C7447 and UDS-19627) show a change in the velocity dispersion in the region of the Balmer break. NMBS-C7447 shows an increase for $\lambda_{\rm start} > 3800$ Å, but decreases after Ca H&K have been removed from the fit. UDS-19627 shows an increase of 50 km s^{-1} when the Balmer break is excluded. When we reduce the red part of the spectrum (Figure 3.12, right panels), we also find a stable fit, except for NMBS-C18265. After excluding Na D from the fit, the velocity dispersion increases by a $\sim$100 km s^{-1}. We think this is because NMBS-C18265 has a more evolved stellar populations than say for example NMBS-C7447. With the Ca H&K lines masked out due to atmospheric absorption, Na D is one of the strongest lines in the spectrum, and its exclusion could explain the sudden change in the measured dispersion.

To summarize, for most galaxies we find only a mild dependence on the wavelength range that is used in the fit. We do find that with decreasing wavelength range, the random error increases. Finally, even in the absence of strong absorption features like Ca H&K, we find similar velocity dispersions as compared to the full range fit. Due to template mismatch, we only fit $\lambda > 4020$ Å in our final results, as is explained in the next section.

3.A.2 Dependence of the velocity dispersion on the template choice

Next, we study how different templates may influence the measured velocity dispersion. We use a sample of BC03 τ-models, as presented in Section 3.3.1. In particular, we are interested in the effect of template age and metallicity. In Figure 3.13 we show the reduced χ^2 from the SPS-modeling, vs. the velocity dispersions measured using this template. The different points

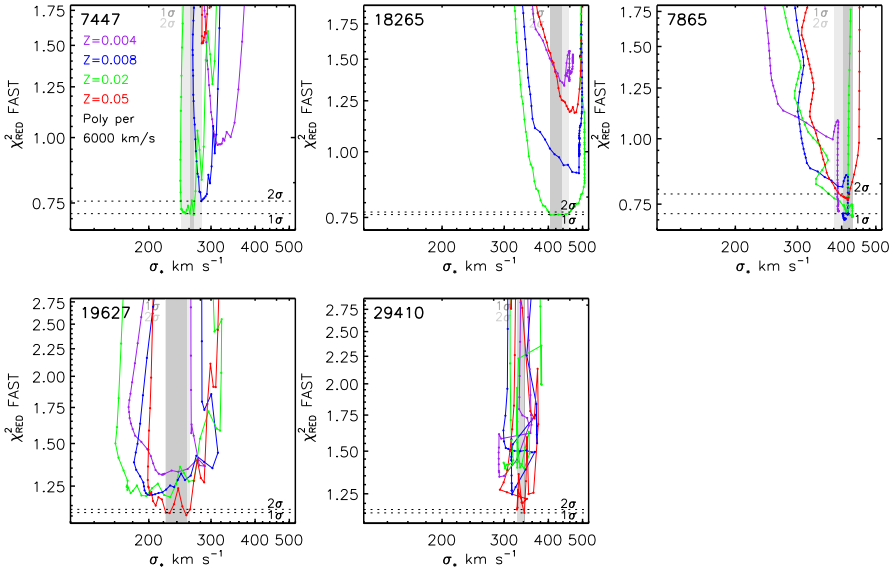

Figure 3.13: Reduced χ^2 from SPS-modeling vs. velocity dispersion for different templates. Different points indicate different template ages, while different colors show different metallicities. All fits are done on the full-wavelength range and with one-order per 6000km s^{-1} for the additive polynomial. The narrower the horizontal distribution is, the more stable the velocity dispersion is. For most sources, we find a stable solution for the velocity dispersion by using different templates, except for UDS-19627, which shows a large range in velocity dispersions.

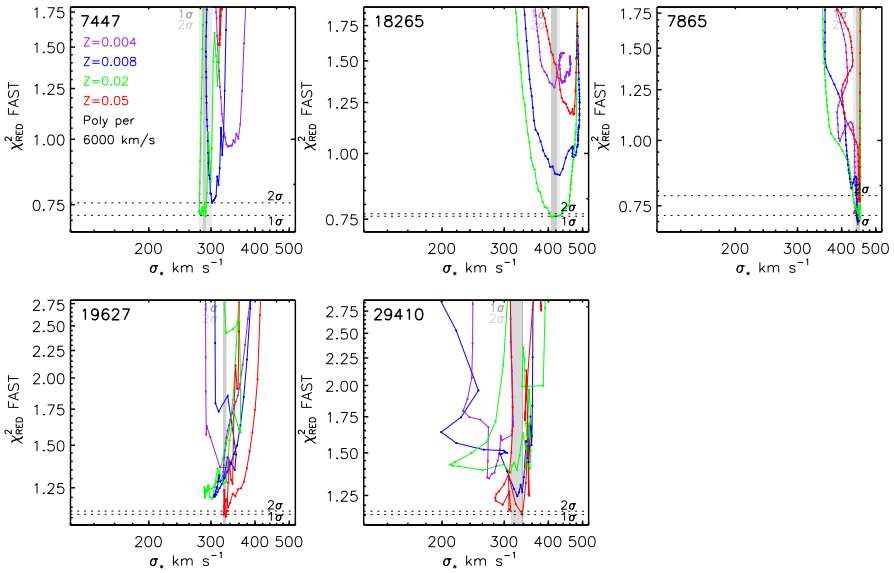

Figure 3.14: Reduced χ^2 vs. velocity dispersion for different templates, similar to Figure 3.13 but now excluding the Balmer break ($\lambda > 4020$ Å). Whereas with the full wavelength range UDS 19627 showed a large variation in the velocity dispersion as a function of template, this time we do find a stable solution, as the distribution is narrower. The other sources also, show a decrease in the uncertainty due to different templates, except for UDS-29410. However, this is due to lower S/N of this spectrum and the shorter fitted wavelength range as before.

represent different ages of the templates, with the minimum χ^2 corresponding to the best-fit age as listed in Table 3.3. The different colors indicate the different metallicities. We show the χ^2 from the SPS-modeling instead of the χ^2 from the dispersion fit, as the former is derived from the full Visual and NIR spectrum plus all the broadband and medium-band photometric data. This large wavelength range yields better constraints for the stellar population, thus larger relative ranges in χ^2 as compared to the χ^2 from the dispersion fit. Also, as we add high-order additive polynomials to the templates from fitting the velocity dispersion (in this case one order per 6 000 km s^{-1}), the effect of different template-ages is mostly washed out, and we get a small relative χ^2.

In Figure 3.13 we see that for most galaxies the velocity dispersion for templates allowed within 2σ gives consistent results. Different metallicities do give different velocity dispersions at their minimum χ^2, but this is a mere reflection of the age-metallicity degeneracy. Different metallicities have different best-fitting ages, which in turn give different velocity dispersion. At a $1-\sigma$ level, we only have a handful of best-fitting templates, for which we obtain similar velocity dispersions. UDS-19627 is the exception, which shows a large dependency of the measured velocity dispersion as a function of template age within the $1-\sigma$ allowed range. At the $1-\sigma$ level, we find a range of ~ 30km s^{-1}, due to template uncertainty, while the random error is one of the lowest, only ~ 30km s^{-1}. Even though templates with χ^2 of 1.20 or higher are statistically considered a bad fit, the large range in the velocity dispersion is worrying. If we could not have constrained the best-fitting template from the full range spectrum and broadband data, the measured velocity dispersion would be highly uncertain.

However, if we exclude the Balmer break from the velocity dispersion fit, the dependency on template age almost completely disappears (Figure 3.14). UDS-19627 shows the most dramatic change, where we suddenly see a tight range of best-fitting velocity dispersions. We do note that the velocity dispersion has increased, as was already shown in Figure 3.12. UDS-29410 appears to have a slightly higher template uncertainty if we only fit for $\lambda > 4020$ Å, but this is driven by the lower S/N of the spectrum as we now use a shorter wavelength range.

To conclude, we find a systematic uncertainty due to templates with different ages. This is caused by the Balmer break, present in the relatively young galaxies in our sample. By only fitting for $\lambda > 4020$ Å, the uncertainty due to template mismatch almost completely disappears. In that case, templates with different metallicities do give different velocity dispersions, but this is most likely caused by the underlying age-metallicity degeneracy.

3.A.3 Dependence of the velocity dispersion on the order of the additive polynomial

In order to correct for stellar continuum emission differences between the observed galaxy spectrum and the template, we use an additive Legendre polynomial. If we would not apply such a correction, the fitting routine could try to correct for this discrepancy by changing the velocity dispersion. Values that are typically used in the literature vary from 5000 to 15000 km s^{-1} per order. We do not use multiplicative Legendre polynomials, because the S/N of the spectra are too low, and it would add another degree of uncertainty to the fit. Here, we test the influence of the additive polynomial to our measured velocity dispersions. Again we use the best-fit τ-model as a template while varying the additive polynomials from 0 to 50. We fit both the full-wavelength range and the wavelength range with $\lambda > 4020$ Å.

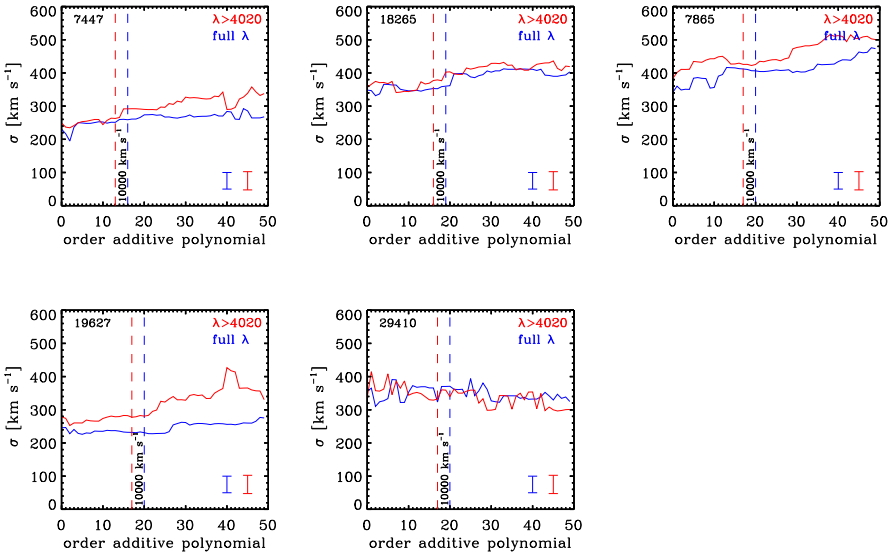

Figure 3.15: Velocity dispersion as measured with different order additive polynomials. The full-wavelength range fit is shown in blue, while the fit with $\lambda > 4020$ Å is shown in red. We find an increase of the velocity dispersion with increasing order. The fit is most stable when using a polynomial with order between 10 and 30. The vertical dashed lines shows the order that corresponds to 10000 km s^{-1}, the polynomial that we use for obtaining science results.

Figure 3.15 shows the results, with the blue line representing the full-wavelength fit, while the red line shows the results for $\lambda > 4020$ Å. The vertical dashed line indicates the polynomial with one order per 10000 km s^{-1}. Overall we find that by increasing the additive polynomial, the measured velocity dispersion increases. In general we find that between polynomials of 10 and 30, the smallest increase in the velocity dispersion occurs, and this appears to be the most stable region. For this reason, we use one order per 10000 km s^{-1} for our science results.

3.A.4 Systematic errors on the velocity dispersion at low signal-to-noise

While it is clear that a decrease in the S/N of the spectra will increase the random errors on the velocity dispersion, it could also cause systematic offsets (e.g., see Franx et al. 1989). A concern would be that low S/N would lead to an overestimate of the velocity dispersions. Therefore, in this section we test if there are systematic effects when changing the S/N for each source. The S/N we refer to in this section is derived in the region in which we also fit the velocity dispersion, i.e., $4020\,\text{Å} < \lambda_{\text{rest-frame}} < 7000\,\text{Å}$.

For each source, we calculated the effect of S/N in a similar fashion as we derived the uncertainty on the velocity dispersion in Section 3.3.2. First, we subtracted the best-fit model from the spectrum. This residual now corresponds to the noise for this particular S/N of this source. We multiply this residual by a certain factor to obtain a new (higher or lower) S/N as compared to our reference S/N. These residuals are then randomly rearranged in wavelength space and added to the best-fit template that has been convolved to a velocity dispersion of 300 km s^{-1}. We then determined the velocity dispersion of simulated spectra with this S/N,

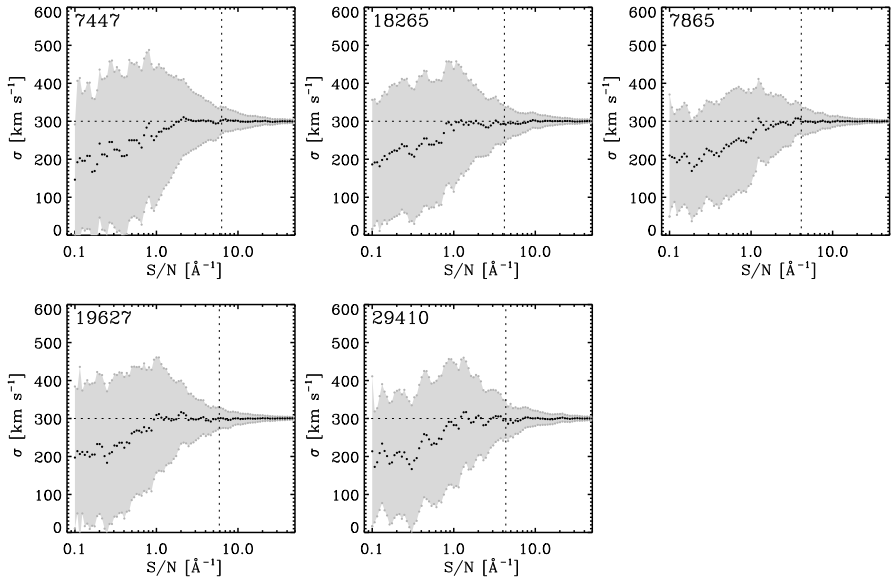

Figure 3.16: Comparison of the recovered velocity dispersion vs. the S/N of simulated spectra. The vertical dashed line shows the original S/N of the spectrum, and the horizontal dashed line shows the input velocity dispersion of 300 km s^{-1}. The black dots show the median of a 100 simulations for each S/N, while the gray area shows the median absolute deviation from these 100 simulations. We find no systematic offset from the input velocity dispersion for S/N $> 1\,\text{Å}^{-1}$, while below this S/N we find that the recovered velocity dispersion is systematically lower.

and repeat this shuffling 100 times. Lastly, we repeat this procedure for a large range in S/N from 0.1 to 100 Å^{-1}. We note that uncertainties due to template mismatch are not included in this analysis.

In Figure 3.16 we show the results, with the different values of the S/N on the horizontal axis. We see that increasing the S/N will also decrease the random error in the velocity dispersions. On average, we find that in order to reach a uncertainty of less than 10% on the velocity dispersion measurement, you need an S/N of $8\,\text{Å}^{-1}$ or higher. NMBS-COS 7865 shows the lowest random error at fixed S/N, which is older stellar population of the galaxy. No systematic offset in the velocity dispersion is found for an S/N of 1Å^{-1}. Below this value, however, we find that the velocity dispersion is systematically underestimated as the S/N decreases, though the offset is still smaller than the random errors. We note that Franx et al. (1989) already presented simple arguments for predicting the systematic error. They show that the systematic offset of the velocity dispersion can be derived from error in the measured velocity, and goes as $\Delta\sigma \propto 0.5dv^2/\sigma$. We verified from these simulations that this is indeed the case. From this analytic approximation, we furthermore conclude that the systematic uncertainties of our measured velocity dispersion are small.

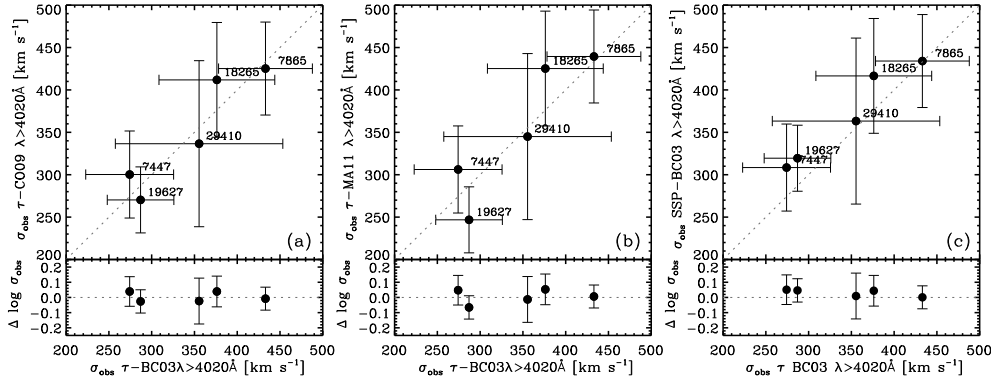

Figure 3.17: Comparison of the velocity dispersion when using different methods. Left panel: velocity dispersion as derived with the models of BC03 and Conroy et al. (2009). Even though the models are based on different stellar libraries with different resolution, the velocity dispersions measured with these models are consistent. Middle panel the same as the left panel but now using BC03 and Maraston & Strömbäck (2011) for comparison. In general, we find consistent results within the errors, but UDS19627 has a lower velocity dispersion when we use the Ma11 models. Right panel: velocity dispersion as derived with optimal template construction vs. the best-fitting τ-model. The optimal template is constructed from BC03 SSP models with a full range in age and metallicity. Dispersions from the optimal template construction are slightly higher, but well within the errors.

3.A.5 Dependence of the velocity dispersion on the SPS models and template construction

Here, we test how our velocity dispersions would change if we make different choices for the SPS-model, and test the difference between a single τ-model and a template constructed from different combinations of singe stellar population (SSP) models. The left and middle panel of Figure 3.17 show what would happen if we would choose the Flexible-SPS models by Conroy et al. (2009, FSPS) or the models by Maraston & Strömbäck (2011, Ma11). These models are based on a different stellar library with slightly higher resolution as compared to BC03, i.e., MILES (Sánchez-Blázquez et al., 2006) vs. STELIB (Le Borgne et al., 2003). If a systematic uncertainty in the measured velocity dispersion is present, for example due to the resolution or details that go into the SPS-models, it would show up in this comparison. We determined a best-fit τ model using the FSPS and Ma11 models in exactly the same way as was done for the BC03 models (see Section 3.3.1). When comparing the velocity dispersions derived by using the BC03 and FSPS τ-models, we do not find any significant difference (left panel of Figure 3.17). In the middle panel we compare Ma11 and BC03. Here too, we find a good correspondence. For UDS19627 the Ma11 models give a lower velocity dispersion, though still within the $1-\sigma$ error. These results confirm that our measurements are stable against the choice of SPS-model and template with different resolution.

Finally, in Figure 3.17 (right panel) we compare the velocity dispersion from the best-fit τ-model, vs. an optimal template constructed by pPXF. This optimal template is built from a full spectral library from BC03 SSP models, with full range in age and metallicity. We note that the optimal template construction only uses the wavelength regime provided in the dispersion fit ($3600\,\text{Å} < \lambda < 7000\,\text{Å}$) , and does not take into account the effects of dust. The velocity dispersions from the optimal templates are slightly higher as compared to the

single τ-model, although it is well below the random error. Interestingly, the galaxy with the largest dust-contribution, NMBS-C18265, also shows the largest difference between the two different fitting techniques. In this chapter, we choose to use the best-fitting $\tau - model$ as the dispersion template, as this is the best representation of the stellar population. As the stellar mass is also based on this τ-model, we use the same stellar population when comparing the stellar to the dynamical mass.

3.B Aperture corrections for velocity dispersion measurements

Here, we investigate the effects of different apertures and extraction methods on the observed velocity dispersion. The standard approach is to use a power-law to scale the observed velocity dispersion, measured within a certain $r_{\rm aper}$, to the velocity dispersion as if measured within $r_{e/8}$, using the following expression by Jorgensen et al. (1995):

$$\frac{\sigma_{\rm aper}}{\sigma_{e/8}} = \left(\frac{r_{\rm aper}}{r_{\rm e}/8}\right)^{-0.04}. \qquad (3.17)$$

Or using a more recent result from the SAURON survey (Cappellari et al., 2006):

$$\frac{\sigma_{\rm aper}}{\sigma_{\rm e}} = \left(\frac{r_{\rm aper}}{r_{\rm e}}\right)^{-0.066\pm0.035}. \qquad (3.18)$$

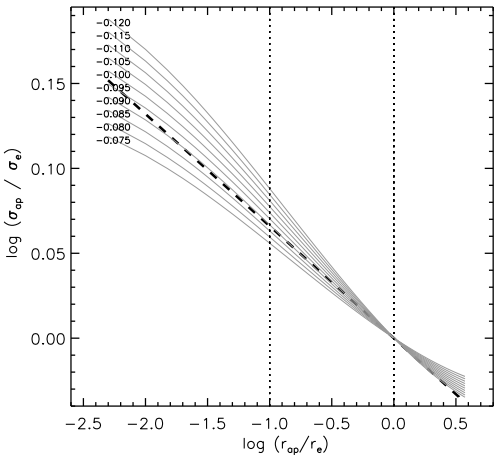

Figure 3.18: Comparison of the observed vs. the analytic kinematic profile. The black dashed line is the observed relation from Cappellari et al. (2006), and is valid between for $-1.0 < \log(r_{\rm aper}/r_{\rm e}) < 0$ using $d = -0.089$, shown as the vertical dashed lines. For different values of d in Equation 3.19, we evaluated Equation 3.20 which is shown as the different gray lines. Between $-1.0 < \log(r_{\rm aper}/r_{\rm e}) < 0$, we find the best match between the observed and analytic kinematic profile when using $d = -0.089$

In the case of Jorgensen et al. (1995), the velocity dispersions have been measured in the range of $-1.5 < \log(r_{\rm aper}/r_{\rm e}) < -0.5$, and for Cappellari et al. (2006) for $-1.0 < \log(r_{\rm aper}/r_{\rm e}) < 0$. In this work however, we are outside this range with $\log(r_{\rm aper}/r_{\rm e}) > 0.5$, that is $r_{\rm e}$ being much smaller than $r_{\rm aper}$. Also, the galaxies in our sample have effective radii much smaller than the FWHM of the PSF, which is why the standard approach most likely will not be valid. We analyze this problem in two steps. Firstly, we use an analytic description for the kinematic profile and match this to the observed relation as found by Cappellari et al. (2006). Secondly, using our model we study the behavior of the observed velocity dispersion for different apertures (both circular and non-circular) and different FWHM for the PSF. Our reference model will be a circular aperture with size $r_{\rm e}$, without the effects of seeing.

A good description of the kinematic profile for early galaxies is given by (see e.g., Treu et al. 1999; Bertin et al. 2002) :

$$\sigma(r) = \left(\frac{r}{r_{\rm e}}\right)^{d} \times \sigma_{\rm cst}, \qquad (3.19)$$

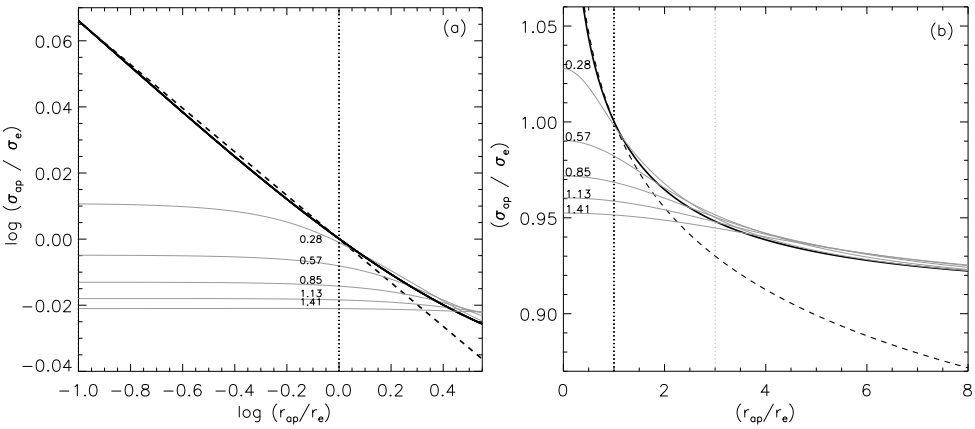

Figure 3.19: Comparison of the observed vs. the analytic kinematic profile, similar to Figure 3.18 but now including the effect of seeing. Panel (a) shows the kinematic in log-log space, while the panel (b) is in linear units. The black dashed line is the observed relation from Cappellari et al. (2006), while the solid black line shows our reference model (no PSF). The gray lines show different assumption for the seeing, where the numbers indicate the FWHM of the PSF in arcsec. The vertical black dotted line shows where $r_{ap} = r_e$, and the vertical gray dotted line shows a typical $r_{\rm aper}/r_e$ for our observations. With increasing FWHM, we find that the kinematic profiles becomes less steep for the inner part, as is expected from the convolution with the PSF. In the outer part of the kinematic profile, we see very little change as compared to our reference model.

with $-0.1 < d < 0$. The observed kinematic profile within a circular aperture will be a projection of $\sigma(r)^2$ and the galaxies intensity profile :

$$\sigma^2(r_{\rm aper}) = \frac{\int_0^{r_{\rm aper}} \sigma^2(r) I_{\rm gal}(r) 2\pi r dr}{\int_0^{r_{\rm aper}} I_{\rm gal}(r) 2\pi r dr}. \tag{3.20}$$

Here, $I_{\rm gal}(r)$ is the Sérsic Profile:

$$I(r) = I_{\rm e} \exp\left\{-b_n \left[\left(\frac{r}{r_{\rm e}}\right)^{1/n} - 1\right]\right\} \tag{3.21}$$

To avoid numerical issues in the center, we approximate Equation 3.19 and Equation 3.21 by:

$$\sigma(r) = \left(\frac{r + r_{\rm core}}{r_{\rm e}}\right)^{d} \times \sigma_{cst}, \tag{3.22}$$

$$I(r) = I_{\rm e} \exp\left\{-b_n \left[\left(\frac{r + r_{\rm core}}{r_{\rm e}}\right)^{1/n} - 1\right]\right\} \tag{3.23}$$

where r_{core} is chosen to be $1/30 r_{\rm e}$. We can estimate the power d by evaluating Equation 3.20 for different values of d and comparing the results to Equation 1 from Cappellari et al. (2006). Figure 3.18 shows the Cappellari et al. (2006) relation (dashed black line) and our model with different values for d, normalized to $r_{\rm e}$ (gray lines). We find a best fitting value for

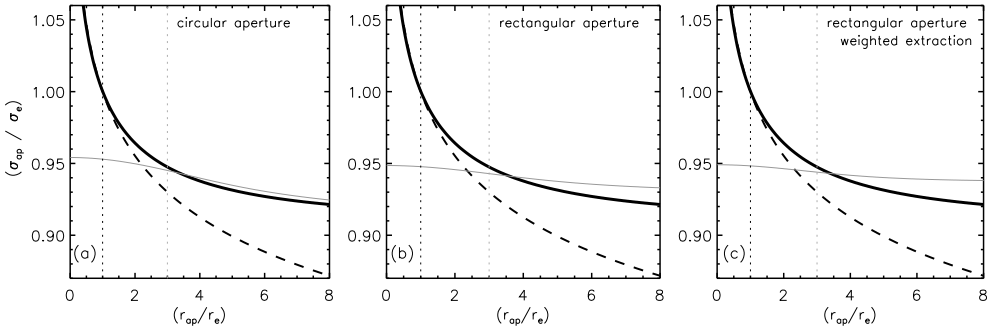

Figure 3.20: Observed kinematic profile in different apertures: circular, rectangular, and rectangular including a weight function according to Equation 3.25. The dashed line is the Cappellari et al. (2006) relation, the solid line is our reference model (circular aperture, no PSF), and the gray line is the modeled kinematic including the effect of the PSF. The vertical gray dashed line shows a typical $r_{\rm aper}/r_{\rm e}$ for our observations. We note that $r_{\rm aper}$ is in the direction along the slit.

$d = -0.089$ in the region of $(-1.0 < \ log(r_{\rm aper}/r_{\rm e}) < 0$. Notice that for $\log(r_{\rm aper}/r_{\rm e}) > 0.0$ our model deviates from the simple power law in Equation 3.19.

Now that we have found the intrinsic kinematic profile, we can explore the influence of the PSF on the observed dispersion. The PSF is modeled using a combination of two Gaussians, where $\sigma_1 = 2\sigma_2$, and both Gaussians having equal flux. This PSF is then convolved with the kinematic and intensity profiles:

$$\sigma^2(r_{\rm aper}) = \frac{\int_0^{r_{\rm aper}} \left\{ \left[\sigma^2(r) I_{\rm gal}(r)\right] \otimes {\rm PSF} \right\}\ 2\pi r dr}{\int_0^{r_{\rm aper}} \left\{ \left[I_{\rm gal}(r)\right] \otimes {\rm PSF} \right\}\ 2\pi r dr}. \tag{3.24}$$

Again we compare the observed kinematic profile from Cappellari et al. (2006) and our analytic results from Equation 3.24, which includes the effect of the PSF, and are shown in Figure 3.19. If we compare the black line, which is our reference model, to the gray lines, which include the effect of the PSF, we see that the inner profile ($\log(r_{\rm aper}/r_{\rm e}) < 0.5$) is mostly affected and the kinematic profile becomes less steep. This is also particularly clear from Figure 3.19b where we see that very little changes for $r_{\rm aper}/r_{\rm e} > 4$ as compared to the reference model.

Instead of using a circular aperture, we now consider the case of a rectangular aperture, similar to what is used in the spectra from X-Shooter. Equation 3.24 can be modified to include a weight function $g(y)$ which is commonly used in optimized extraction. The integral in Equation 3.25 is also replaced by a Riemann sum. In the x direction (slit width) the aperture size is always the same, i.e., 0.″9 for X-Shooter spectra, but the y direction is now parallel to $r_{\rm aper}$:

$$\sigma^2(x_{\rm aper}, y_{\rm aper}) = \frac{\sum_0^{x_{\rm aper}} \sum_0^{y_{\rm aper}} \left\{ \left[\sigma^2(x,y) I_{\rm gal}(x,y)\right] \otimes {\rm PSF} \right\} g(y)\ \Delta x \Delta y}{\sum_0^{x_{\rm aper}} \sum_0^{y_{\rm aper}} \left\{ \left[I_{\rm gal}(x,y)\right] \otimes {\rm PSF} \right\} g(y)\ \Delta x \Delta y}. \tag{3.25}$$

Figure 3.20 shows the difference between using a circular aperture, a rectangular aperture

without a weighting function, and a rectangular aperture including a weighting function. The slit width that was used is 0.″9, with the FWHM of the PSF also being 0.″9. The spectrum was extracted with $r_{\rm aper} = 0.''45$. We see that the correction is slightly higher for the rectangular aperture as compared to the circular aperture at $r_{\rm aper}/r_{\rm e} = 2.25$. The behavior at $r_{\rm aper}/r_{\rm e} > 3$ is very different for the three different cases. When using a rectangular aperture with optimized extraction, the observed profile is flatter as compared to the other models. The corrections are on average between 3% and 5%.

From Figure 3.20, it is clear that by using a simple power law for the aperture correction, we would overestimate the corrections by a large fraction. Furthermore, we have shown that it is vital to use a suitable aperture and include the effects of seeing, especially when $r_{\rm aper}/r_{\rm e} > 2$. The corrections applied to our final results are derived for the rectangular aperture, including a weighting function.

References

Bezanson, R., van Dokkum, P. G., Tal, T., Marchesini, D., Kriek, M., Franx, M., & Coppi, P. 2009, ApJ, 697, 1290
Bezanson, R., van Dokkum, P., van de Sande, J., Franx, M., & Kriek, M. 2013, ApJ, 764, L8
Bertin, E., & Arnouts, S. 1996, A&AS, 117, 393
Bertin, G., Ciotti, L., & Del Principe, M. 2002, A&A, 386, 149
Blakeslee, J. P., Holden, B. P., Franx, M., et al. 2006, ApJ, 644, 30
Blanton, M. R., Schlegel, D. J., Strauss, M. A., et al. 2005, AJ, 129, 2562
Bouwens, R. J., Illingworth, G. D., Oesch, P. A., et al. 2010, ApJ, 709, L133
Brammer, G. B., Whitaker, K. E., van Dokkum, P. G., et al. 2011, ApJ, 739, 24
Brinchmann, J., Charlot, S., White, S. D. M., et al. 2004, MNRAS, 351, 1151
Bruzual, G., & Charlot, S. 2003, MNRAS, 344, 1000
Calzetti, D., Armus, L., Bohlin, R. C., Kinney, A. L., Koornneef, J., & Storchi-Bergmann, T. 2000, ApJ, 533, 682
Cappellari, M., & Emsellem, E. 2004, PASP, 116, 138
Cappellari, M., et al. 2006, MNRAS, 366, 1126
Cappellari, M., et al. 2009, ApJ, 704, L34
Cassata, P., et al. 2010, ApJ, 714, L79
Cenarro, A. J., & Trujillo, I. 2009, ApJ, 696, L43
Chabrier, G. 2003, PASP, 115, 763
Ciotti, L. 1991, A&A, 249, 99
Conroy, C., Gunn, J. E., & White, M. 2009, ApJ, 699, 486
Daddi, E., et al. 2005, ApJ, 626, 680
D'Odorico, S., et al. 2006, Proc. SPIE, 6269,98
Feldmann, R., Carollo, C. M., Mayer, L., et al. 2010, ApJ, 709, 218
Ferré-Mateu, A., Vazdekis, A., Trujillo, I., et al. 2012, MNRAS, 423, 632
Förster Schreiber, N. M., Franx, M., Labbé, I., et al. 2006, AJ, 131, 1891
Franx, M., Illingworth, G., & Heckman, T. 1989, ApJ, 344, 613
Franx, M., van Dokkum, P. G., Schreiber, N. M. F., Wuyts, S., Labbé, I., & Toft, S. 2008, ApJ, 688, 770
Goldoni, P., Royer, F., François, P., Horrobin, M., Blanc, G., Vernet, J., Modigliani, A., & Larsen, J. 2006, Proc. SPIE, 6269,80
Grogin, N. A., Kocevski, D. D., Faber, S. M., et al. 2011, ApJS, 197, 35
Hilz, M., Naab, T., & Ostriker, J. P. 2012, arXiv:1206.5004
Hopkins, P. F., Hernquist, L., Cox, T. J., Keres, D., & Wuyts, S. 2009a, ApJ, 691, 1424
Hopkins, P. F., Bundy, K., Murray, N., et al. 2009b, MNRAS, 398, 898
Jorgensen, I., Franx, M., & Kjaergaard, P. 1995, MNRAS, 276, 1341
Kauffmann, G., Heckman, T. M., White, S. D. M., et al. 2003, MNRAS, 341, 33
Koekemoer, A. M., Aussel, H., Calzetti, D., et al. 2007, ApJS, 172, 196
Koekemoer, A. M., Faber, S. M., Ferguson, H. C., et al. 2011, ApJS, 197, 36
Kormendy, J., Fisher, D. B., Cornell, M. E., & Bender, R. 2009, ApJS, 182, 216
Kriek, M., et al. 2006, ApJ, 649, L71
Kriek, M., van Dokkum, P. G., Labbé, I., Franx, M., Illingworth, G. D., Marchesini, D., & Quadri, R. F. 2009, ApJ, 700, 221 1
Labbé, I., et al. 2005, ApJ, 624, L81
Lawrence, A., Warren, S. J., Almaini, O., et al. 2007, MNRAS, 379, 1599
Le Borgne, J.-F., Bruzual, G., Pelló, R., et al. 2003, A&A, 402, 433
Maraston, C., & Strömbäck, G. 2011, MNRAS, 418, 2785
Markwardt, C. B. 2009, Astronomical Data Analysis Software and Systems XVIII, 411, 251
Martinez-Manso, J., Guzman, R., Barro, G., et al. 2011, ApJ, 738, L22
Massey, R., Stoughton, C., Leauthaud, A., et al. 2010, MNRAS, 401, 371
Munari, U., Sordo, R., Castelli, F., & Zwitter, T. 2005, A&A, 442, 1127
Muzzin, A., Marchesini, D., van Dokkum, P. G., et al. 2009, ApJ, 701, 1839
Naab, T., Johansson, P. H., & Ostriker, J. P. 2009, ApJ, 699, L178
Newman, A. B., Ellis, R. S., Treu, T., & Bundy, K. 2010, ApJ, 717, L103
Onodera, M., Renzini, A., Carollo, M., et al. 2012, arXiv:1206.1540
Oser, L., Ostriker, J. P., Naab, T., Johansson, P. H., & Burkert, A. 2010, ApJ, 725, 23
Oser, L., Naab, T., Ostriker, J. P., & Johansson, P. H. 2012, ApJ, 744, 63

Patel, S. G., van Dokkum, P. G., Franx, M., et al. 2012, arXiv:1208.0341
Peng, C. Y., Ho, L. C., Impey, C. D., & Rix, H.-W. 2010, AJ, 139, 2097
Salim, S., Rich, R. M., Charlot, S., et al. 2007, ApJS, 173, 267
Sánchez-Blázquez, P., et al. 2006, MNRAS, 371, 703
Saracco, P., Gargiulo, A., & Longhetti, M. 2012, MNRAS, 422, 3107
Sérsic, J. L. 1968, Cordoba, Argentina: Observatorio Astronomico, 1968,
Shen, S., Mo, H. J., White, S. D. M., Blanton, M. R., Kauffmann, G., Voges, W., Brinkmann, J., & Csabai, I. 2003, MNRAS, 343, 978
Skelton, R. et al. in preparation
Szomoru, D., et al. 2010, ApJ, 714, L244
Szomoru, D., Franx, M., & van Dokkum, P. G. 2012, ApJ, 749, 121
Taylor, E. N., Franx, M., Glazebrook, K., et al. 2010a, ApJ, 720, 723
Taylor, E. N., Franx, M., Brinchmann, J., van der Wel, A., & van Dokkum, P. G. 2010b, ApJ, 722, 1
Toft, S., Gallazzi, A., Zirm, A., et al. 2012, ApJ, 754, 3
Treu, T., Stiavelli, M., Casertano, S., Møller, P., & Bertin, G. 1999, MNRAS, 308, 1037
Treu, T., Ellis, R. S., Liao, T. X., & van Dokkum, P. G. 2005a, ApJ, 622, L5
Treu, T., Ellis, R. S., Liao, T. X., et al. 2005b, ApJ, 633, 174
Trujillo, I., et al. 2006, MNRAS, 373, L36
Trujillo, I., Cenarro, A. J., de Lorenzo-Cáceres, A., et al. 2009, ApJ, 692, L118
van de Sande, J., Kriek, M., Franx, M., et al. 2011, ApJ, 736, L9
van Dokkum, P. G. 2001, PASP, 113, 1420
van Dokkum, P. G., et al. 2008, ApJ, 677, L5
van Dokkum, P. G., Kriek, M., & Franx, M. 2009, Nature, 460, 717
van Dokkum, P. G., et al. 2010, ApJ, 709, 1018
van der Wel, A., Franx, M., van Dokkum, P. G., & Rix, H.-W. 2004, ApJ, 601, L5
van der Wel, A., Franx, M., van Dokkum, P. G., et al. 2005, ApJ, 631, 145
van der Wel, A., Holden, B. P., Zirm, A. W., et al. 2008, ApJ, 688, 48
van der Wel, A., Bell, E. F., van den Bosch, F. C., Gallazzi, A., & Rix, H.-W. 2009, ApJ, 698, 1232
Vernet, J., Dekker, H., D'Odorico, S., et al. 2011, A&A, 536, A105
Villumsen, J. V. 1983, MNRAS, 204, 219
Warren, S. J., Hambly, N. C., Dye, S., et al. 2007, MNRAS, 375, 213
Whitaker, K. E., et al. 2010, ApJ, 719, 1715
Whitaker, K. E., Labbé, I., van Dokkum, P. G., et al. 2011, ApJ, 735, 86
Whitaker, K. E., Kriek, M., van Dokkum, P. G., et al. 2012, ApJ, 745, 179
Williams, R. J., Quadri, R. F., Franx, M., van Dokkum, P., & Labbé, I. 2009, ApJ, 691, 1879
Wuyts, S., van Dokkum, P. G., Kelson, D. D., Franx, M., & Illingworth, G. D. 2004, ApJ, 605, 677
Wuyts, S., Labbé, I., Schreiber, N. M. F., et al. 2008, ApJ, 682, 985